NEUROSCIENCE

Astrocytes control quiescent NSC reactivation via GPCR signaling–mediated F-actin remodeling

Kun-Yang Lin[1], Mahekta R. Gujar[1], Jiaen Lin[1], Wei Yung Ding[1], Jiawen Huang[1], Yang Gao[1], Ye Sing Tan[1], Xiang Teng[2], Low Siok Lan Christine[2], Pakorn Kanchanawong[2], Yusuke Toyama[2,3], Hongyan Wang[1,4,5]*

Copyright © 2024 The Authors, some rights reserved; exclusive licensee American Association for the Advancement of Science. No claim to original U.S. Government Works. Distributed under a Creative Commons Attribution NonCommercial License 4.0 (CC BY-NC).

The transitioning of neural stem cells (NSCs) between quiescent and proliferative states is fundamental for brain development and homeostasis. Defects in NSC reactivation are associated with neurodevelopmental disorders. *Drosophila* quiescent NSCs extend an actin-rich primary protrusion toward the neuropil. However, the function of the actin cytoskeleton during NSC reactivation is unknown. Here, we reveal the fine filamentous actin (F-actin) structures in the protrusions of quiescent NSCs by expansion and super-resolution microscopy. We show that F-actin polymerization promotes the nuclear translocation of myocardin-related transcription factor, a microcephaly-associated transcription factor, for NSC reactivation and brain development. F-actin polymerization is regulated by a signaling cascade composed of G protein–coupled receptor Smog, G protein α_q subunit, Rho1 guanosine triphosphatase, and Diaphanous (Dia)/Formin during NSC reactivation. Further, astrocytes secrete a Smog ligand folded gastrulation to regulate Gα_q-Rho1-Dia–mediated NSC reactivation. Together, we establish that the Smog-Gα_q-Rho1 signaling axis derived from astrocytes, an NSC niche, regulates Dia-mediated F-actin dynamics in NSC reactivation.

INTRODUCTION

Tissue development and homeostasis rely on the ability of stem cells to switch between quiescent and proliferative states. Most of neural stem cells (NSCs) in the adult mammalian brain remain in a quiescent state, which, upon physiological stimulation, are reactivated for adult neurogenesis and neural regeneration (*1*). Increasing evidence suggests that defects in NSC reactivation may be associated with aging-related cognitive decline (*2*) and neurodevelopmental disorders, such as microcephaly (*3*). Deciphering the molecular mechanisms underlying NSC reactivation will provide important insights into brain development and regeneration and may facilitate the development of therapeutics for the treatment of brain aging, injury, and neurological disorders.

NSCs in the *Drosophila* larval brain have emerged as an ideal in vivo model to investigate the molecular mechanisms underlying the transition between quiescent and proliferative states. *Drosophila* NSCs are programmed to enter the quiescent state at the end of embryogenesis (*4*), after which they undergo reactivation (undergo cell cycle reentry and growth) within ~24 hours in the early larval stages upon feeding (Fig. 1A) (*4*). Dietary amino acids stimulate the secretion of insulin-like peptides in the brain-blood barrier (BBB) glial cells, an NSC niche in *Drosophila* larval brains; the insulin-like peptides activate the evolutionarily conserved insulin/insulin-like growth factor 1 (IGF-1) signaling (*5*, *6*), which triggers NSC reactivation. Similar to *Drosophila* NSCs, mammalian NSCs are also activated by IGF-1 signaling, and mutations in the human IGF-1 receptor are linked to microcephaly (*7*, *8*). In the mammalian brain, astrocytic glia produce IGF-1 for the proliferation of NSCs (*9*, *10*). In addition, intrinsic factors required for NSC reactivation have also been identified, such as spindle matrix proteins (*11*), striatin-interacting phosphatase and kinase family proteins (*12*), Hsp83 (*13*), CRL4^{Mahj} E3 ubiquitin ligase (*14*), Pr-set7 (*15*), and microtubule-binding proteins Msps and Arf1 (*16*, *17*). On the contrary, the activation of the evolutionarily conserved Hippo pathway keeps NSCs in quiescence (*18*, *19*).

One hallmark of quiescent NSCs (qNSCs) in *Drosophila* is the presence of a primary cellular protrusion that extends from the cell body toward the neuropil. Recently, our laboratory demonstrated that this protrusion is enriched with the actin cytoskeleton (*11*). Although actin cytoskeleton is critical for the asymmetric division and cytokinesis of neural progenitors/stem cells (*20*, *21*), actin dynamics in qNSCs and their potential role in regulating NSC quiescence or reactivation have not been established. Diaphanous (Dia)/Formin family proteins are key regulators of actin dynamics that accelerate filamentous actin (F-actin) nucleation and assembly (*22*). At the barbed end of the F-actin filaments, actin polymerization factor Formins recruit and nucleate monomeric actin (also known as globular actin or G-actin) for filament elongation (*22*). Variants of Dia-related formin 1 (DIAPH1) have been identified in human patients with microcephaly (*23*, *24*). Understanding whether and how Formin-mediated actin dynamics regulate NSC reactivation will provide insights into developing therapeutic targets for neurodevelopmental disorders.

The heterotrimeric G protein complex is composed of three subunits, the α (Gα), β (Gβ), and γ (Gγ) subunits. Upon binding of ligand to the G protein–coupled receptor (GPCR), Gα dissociates from the Gβγ subunits and gets activated. A dysfunction in GPCR signaling is associated with brain aging and neurodegenerative diseases (*25*, *26*). Variants of GPCRs have also been identified in neurodevelopmental disorders including microcephaly (*27*–*29*). In human embryonic kidney (HEK) 293T cells, G protein α_q subunit (Gα_q) interacts with and regulates the activity of the small guanosine

[1]Neuroscience and Behavioral Disorders Programme, Duke-NUS Medical School, 8 College Road, Singapore 169857, Singapore. [2]Mechanobiology Institute, Level 5, T-lab Building, 5A Engineering Drive 1, Singapore, 117411, Singapore. [3]Department of Biological Sciences, National University of Singapore, 14 Science Drive 4, Singapore, 117543, Singapore. [4]Department of Physiology, Yong Loo Lin School of Medicine, National University of Singapore, Singapore 117597, Singapore. [5]Integrative Sciences and Engineering Programme, National University of Singapore, 28 Medical Drive, Singapore 117456, Singapore.
*Corresponding author. Email: hongyan.wang@duke-nus.edu.sg

triphosphatase (GTPase) RhoA (*30*), which, in turn, activates Formins to transduce extracellular stimuli into the assembly and organization of the actin cytoskeleton (*31*). Moreover, gain-of-function variants of G Protein Subunit Alpha Q (GNAQ)/$G\alpha_q$ have been identified in Sturge-Weber syndrome with neurological deficits, e.g., macrocephaly and seizures. Given the major roles of G protein signaling in fundamental cellular processes, the GPCR family has become a major drug target for treatments of various human diseases; 34% of US Food and Drug Administration–approved drugs target GPCRs (*32*). Therefore, understanding how GPCR signaling controls NSC reactivation may provide a potential strategy for the treatment of neurodevelopmental disorders.

Here, we unveiled the fine structure of the actin cytoskeleton and the retrograde flow of F-actin patches in qNSCs. We showed that GPCR Smog-$G\alpha_q$ signaling regulates qNSC reactivation through Rho1-Dia–mediated actin dynamics. Moreover, the microcephaly-like phenotype of *dia* mutants could be suppressed by overexpression of the transcription factor Mrtf (myocardin-related transcription factor) that is controlled by actin dynamics. We further identified astrocyte-like glia as a new NSC niche to produce folded gastrulation (Fog), a ligand of GPCR Smog, for qNSC reactivation. Our study demonstrates a new paradigm of NSC reactivation through astrocyte-mediated activation of GPCR signaling and regulation of actin dynamics.

RESULTS

The dynamics of F-actin filaments and patches in qNSCs

Previously, we showed that F-actin is enriched in the primary protrusion of qNSCs (*11*); however, the dynamics, structure, and function of the actin cytoskeleton in qNSCs are unknown. To examine the structure of F-actin in qNSCs, we expressed the F-actin–binding protein green fluorescent protein–Moesin (GFP-Moe) using an NSC-specific GAL4 driver, *grainy head(grh)–GAL4*, in the NSCs of the *Drosophila* larva brain. As it is challenging to observe the fine structures (4 to 5 μm in diameter) of F-actin in qNSCs, we imaged GFP-Moe using structured illumination microscopy (SIM) (*33*). We further enhanced imaging resolution using expansion microscopy (ExM) (*34*) for isotropic expansion of the fluorescent signal along with the expansion of sample structures (Fig. 1B). Compared with conventional confocal microscopy (*11*), ExM-SIM imaging greatly improved the resolution of F-actin structures in qNSCs (Fig. 1C). Notably, F-actin was observed as long, twisted filaments in the primary protrusion (yellow arrows) and shorter filaments in the soma of qNSCs (Fig. 1C, yellow arrows). In addition, the soma also contained F-actin patches along the filaments (Fig. 1C, red arrows). Our orthogonal view (Fig. 1, D and E) and three-dimensional (3D) reconstruction images (Fig. 1F and movie S1) pointed out a predominantly cortical localization of F-actin in the soma of qNSCs. Next, we used live-cell imaging to monitor F-actin dynamics, marked by GFP-Moe, in qNSCs. At 6-hour after larval hatching (ALH), F-actin patches in the soma underwent robust remodeling (Fig. 1G, red arrows, and movie S2), as F-actin patches in the primary protrusion appeared to move in a retrograde flow toward the soma (Fig. 1H, thermal video stills, white arrows, stills 03:01 to 03:18 and 03:47 to 04:27; and movie S2).

To understand whether this dynamics in the protrusion is important for F-actin polymerization in the soma of qNSCs, we examined F-actin dynamics labeled by GFP::utrophin actin-binding domain (GFP:utABD), followed by the severing of the protrusion using picolaser-induced ablation (movie S3; see Methods for laser setting) (*17*). As expected, GFP::utABD was not recovered at 10 min after injury (Fig. 1I), as opposed to its rapid recovery in the fluorescence recovery after photobleaching (FRAP) experiment (fig. S1, A and B; 50% recovery at 100 s after photobleaching). F-actin patches in the soma diminished markedly after injury to the protrusion (Fig. 1, I and J, and movie S4), suggesting that F-actin patches might move from the protrusion back to the soma in qNSCs.

Dynamics of the actin cytoskeleton during qNSC reactivation

Actin dynamics during the asymmetric division of proliferative NSCs has been well characterized (*20*, *21*, *35*, *36*). However, F-actin dynamics during the switch between quiescent and proliferative states is unknown. As GFP-Moe did not survive beyond 24 hours of ALH, likely due to toxicity of GFP-Moe overexpression, GFP::utABD that survived to adult stages was used to mark F-actin dynamics during qNSC reactivation. Up to 10 hours of ALH, F-actin patches in the primary protrusion moved retrogradely toward the soma (Fig. 1K, 06:30 to 10:42 hh:mm ALH, and movie S5), similar to the retrograde flow seen using GFP-Moe–marked F-actin in qNSCs. Notably, GFP::utABD signal diminished from the distal end of the protrusion (10:56 hh:mm ALH, white arrow) and subsequently disappeared from the entire protrusion (10:42 to 10:56 hh:mm ALH), which was associated with a marked reduction in the number of F-actin patches in the soma of NSCs (red arrows) and an enrichment of F-actin at the apical region of the NSCs (Fig. 1K, black arrow; 10:56 hh:mm ALH; and movie S5). As the NSC reentered into the cell cycle to generate two daughter cells (Fig. 1K, 11:10 hh:mm ALH, and movie S5), F-actin accumulated in the cleavage furrow, as expected, during cytokinesis (Fig. 1K, 11:10 hh:mm ALH, white arrow). Following the division, F-actin patches reappeared in the soma and the protrusion, with the latter attached to the presumptive basal daughter cell–ganglion mother cell (Fig. 1K, 11:52 hh:mm ALH, and movie S5). While the protrusion in qNSCs persisted throughout the first cell division, it underwent a thinning process (*17*, *37*), possibly due to loss of F-actin patches during the reactivation.

Together, our ExM-SIM imaging has clearly demonstrated the presence of fine F-actin structures in qNSCs. Our live imaging analysis suggested that F-actin patches can move from the protrusion to the soma in qNSCs.

Depletion of *diaphanous* causes microcephaly-like phenotype and defects in qNSC reactivation

To identify actin regulators that are involved in qNSC reactivation, we tested whether Dia, the sole Formin in *Drosophila*, is required for NSC reactivation. At 24-hour ALH, most of qNSCs in control larval brains reentered into cell cycle and incorporated 5-ethynyl-2′-deoxyuridine (EdU), with only 17.9% of NSCs remaining quiescent and negative for EdU (Fig. 2, A and B). In contrast, the percentage of qNSCs that were EdU-negative notably increased to 42.7 to 69.5% in two loss-of-function alleles, dia^{1} and dia^{5}, and two hemizygous *dia* mutants, $dia^{1/Df(2L)ED1317}$ and $dia^{5/Df(2L)ED1317}$ (Fig. 2, A and B). In addition, the percentage of qNSCs carrying primary protrusions, the hallmark of qNSCs, increased notably from 5.8% in the control to 15.1 and 16.3% in the dia^{1}- and dia^{5}-mutant brains, respectively (Fig. 2, C and D). Dia

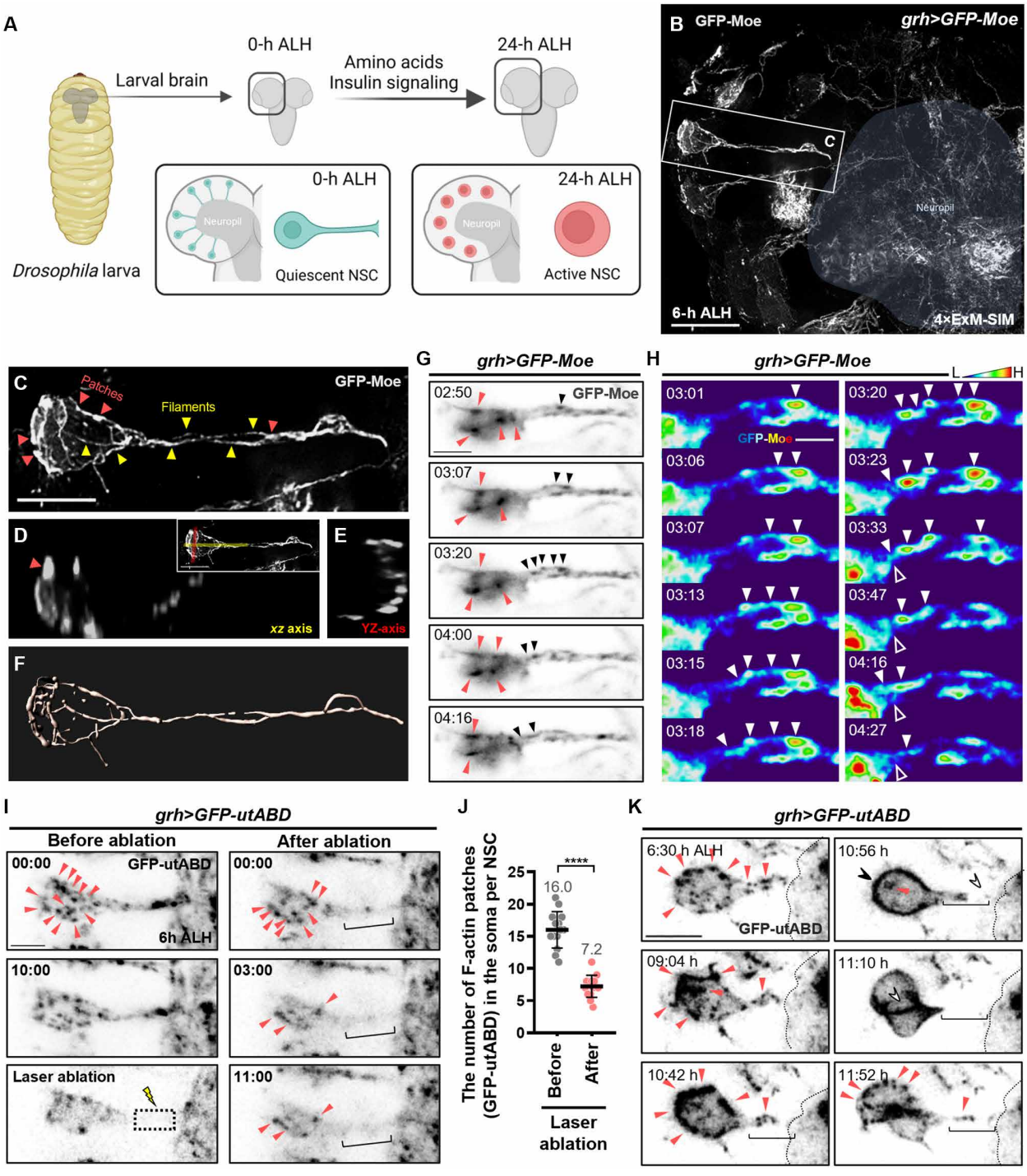

Fig. 1. F-actin structures and dynamics during qNSC reactivation. (**A**) Schematic diagram of qNSC reactivation in the *Drosophila* larva brain. (**B**) Super-resolution imaging of F-actin structure achieved by ExM-SIM microscopy in *Drosophila* larval brain at 6-hour ALH. GFP-Moe (white) marks F-actin. Blue patches, neuropil region. (**C**) High magnification of qNSC from (B). Yellow arrows, F-filaments; red arrows, F-actin patches. (**D** and **E**) Orthogonal view (*xz* axis, D; *yz* axis, E) of qNSC in (C). Insert of (D) shows sections used in (D) (*xz* axis in yellow) and (E) (*yz* axis in red). (**F**) 3D reconstruction of (D). (**G**) Live imaging stills of F-actin dynamics (GFP-Moe, black) in the qNSC at 6-hour ALH. Time, mm:ss. F-actin patches, red arrows; black arrows, retrograde flow of F-actin patches in the protrusion. (**H**) Stills of live imaging of F-actin dynamics (GFP-Moe) in (G) in thermal theme. H, high in thermal scale; L, low in the thermal scale; white arrows, F-actin patches; open arrow, protrusion initiation segment (PIS) region. (**I**) Time-lapse images of GFP-utABD (black) driven by *grh-GAL4* were taken before and after laser ablation. Dashed square, ablated area; red arrows, soma F-actin patches; brackets, the position of primary protrusion of qNSCs. (**J**) Quantification graph of soma F-actin patches of qNSCs before and after laser ablation. Before laser ablation: 16.0 ± 2.8, $n = 14$; after laser ablation: 7.2 ± 1.7, $n = 14$. Student's t test is used for statistics. ****$P < 0.0001$. The means of analyzed phenotypes were shown above each column. (**K**) Live imaging of GFP-utABD (black, F-actin) driven by *grh-GAL4*. Time, hh:mm. Red arrows, F-actin patches; black arrows, apical F-actin; white arrows, absence of F-actin; bracket, primary protrusion. Dashed lines indicate the boundary of neuropil. Scale bars, 10 μm (B and K), 5 μm (C, G, and I), and 2 μm in (H).

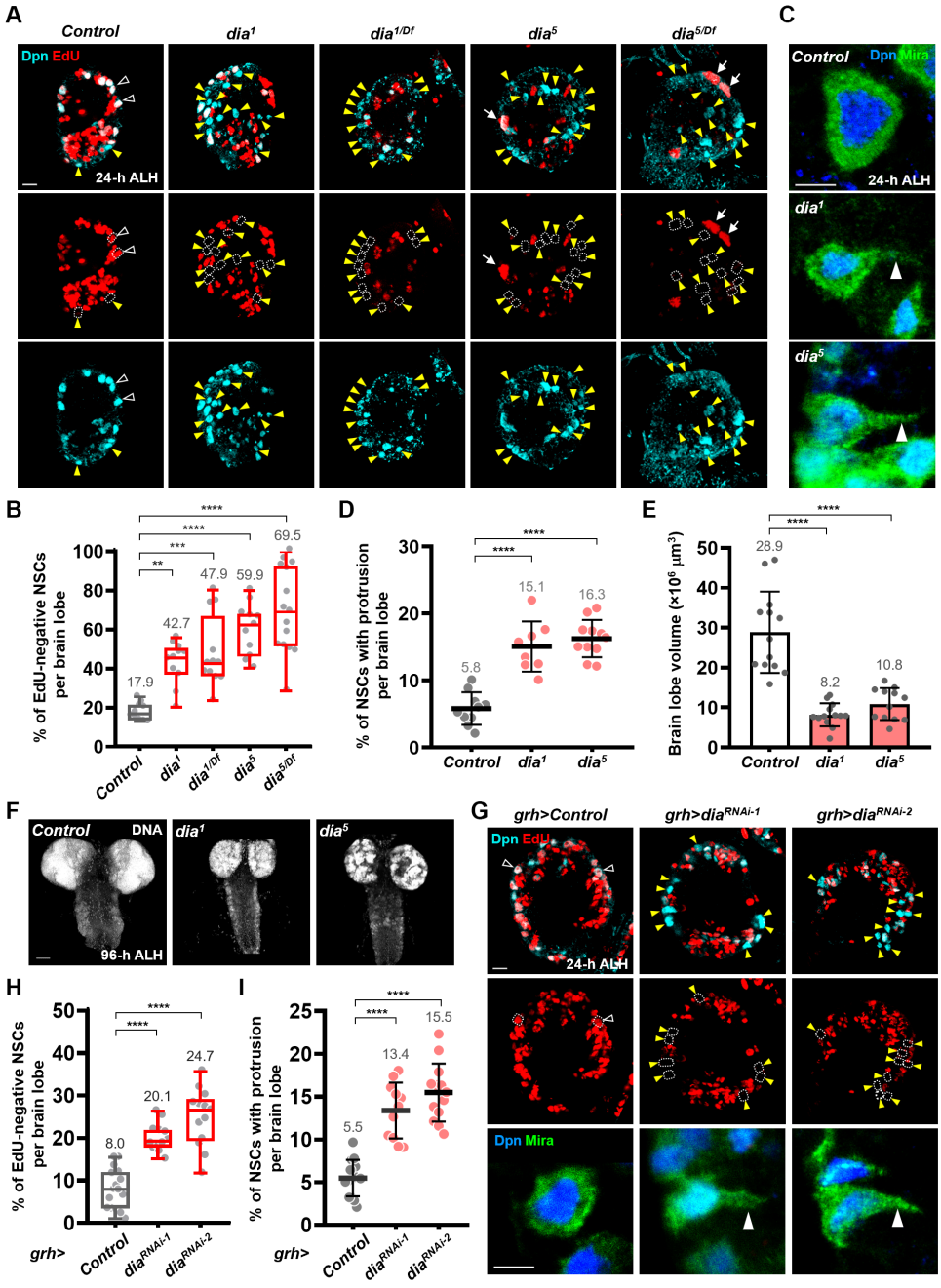

Fig. 2. The actin polymerization factor Dia/Formin is required for qNSC reactivation and brain development. (**A**) Larval NSCs were labeled with EdU and Dpn at 24-hour ALH. Yellow arrows and dashed circles point to EdU-negative NSCs. White arrows, EdU-positive NSCs. White arrows, NSCs with cytokinesis defects (large multi-nucleated cells). (**B**) The quantification graph of EdU-negative NSCs in (A). *Control (yw)*: 17.9 ± 4.4, $n = 10$; dia^{1}: 42.7 ± 10.9, $n = 11$; $dia^{1/Df}$: 47.9 ± 18.0, $n = 12$; dia^{5}: 59.9 ± 13.1, $n = 11$; $dia^{5/Df}$: 69.5 ± 21.6, $n = 15$. (**C**) NSCs were stained for Dpn and Miranda (Mira). White arrows point to primary protrusion of qNSCs. (**D**) Quantification graph of the percentage of NSCs carrying primary protrusion. *Control (yw)*: 5.8 ± 2.4, $n = 10$; dia^{1}: 15.1 ± 3.7, $n = 8$; dia^{5}: 16.3 ± 2.8, $n = 11$. (**E**) The quantification graph of brain volume. *Control (yw)*: 28.9 ± 10.2, $n = 13$; dia^{1}: 8.2 ± 2.9, $n = 13$; dia^{5}: 10.8 ± 4.0, $n = 12$. (**F**) The size of larval brains (DNA, gray). (**G**) Top and middle rows: Proliferating NSCs (Dpn, cyan; EdU, red) in control (β-gal^{RNAi}) or *dia*-KD larval brains (driven by *grh*-GAL4). Yellow arrows, EdU-negative NSCs; white open arrows, EdU^{+} proliferative NSCs. Bottom row: NSCs labeled with Dpn/Mira. White solid arrows, primary protrusion of qNSCs. (**H**) The quantification graph of EdU-negative NSCs. *Control* (β-gal^{RNAi}): 8.0 ± 4.7, $n = 16$; $dia^{RNAi\text{-}1}$: 20.1 ± 3.3, $n = 12$; $dia^{RNAi\text{-}2}$: 24.7 ± 6.7, $n = 13$. (**I**) Quantification graph of the percentage of NSCs retaining primary protrusion. *Control* (β-gal^{RNAi}): 5.5 ± 2.1, $n = 14$; $dia^{RNAi\text{-}1}$: 13.4 ± 3.3, $n = 11$; $dia^{RNAi\text{-}2}$: 15.5 ± 3.4, $n = 13$. One-way analysis of variance (ANOVA) is used for statistics. ****$P < 0.0001$; ***$P < 0.001$; **$P < 0.01$. The means of analyzed phenotypes were shown above each column. Scale bars, 50 μm (F), 10 μm [A and G (top row)], and 5 μm [C and G (bottom row)].

protein levels were diminished in the cytosol of *dia*^{5}-mutant NSCs and *dia*–knockdown (KD) NSCs, while Dia was sequestered in the nucleus of *dia*^{1}-mutant NSCs, resulting in a mild reduction of Dia in the cytoplasm (fig. S2, A to C). Variants of *DIAPH1*, the ortholog of *Drosophila dia* in humans, have been identified in patients with microcephaly (*23*, *24*, *38*). Consistent with this, the volumes of *dia*^{1} and *dia*^{5} brain lobes were markedly reduced to 28 and 37.5%, respectively, compared with the control (100%) at 96-hour ALH (Fig. 2, E and F), suggesting that *Drosophila dia* mutants also display a microcephaly-like phenotype. *Dia* RNA interference (RNAi) in NSCs under the control of *grh-GAL4* also resulted in defects in NSC reactivation (Fig. 2, G to I), suggesting that Dia is required intrinsically in the NSCs for their reactivation. Likewise, knocking down *dia* via another NSC driver, *inscuteable-GAL4* driver (*insc-GAL4*), resulted in NSC reactivation defect (fig. S4, A and B). In contrast, *dia* KD in glial cells or fat body did not cause any reactivation defect (fig. S5). Our results suggest that the actin polymerization factor Dia is a novel intrinsic regulator of qNSC reactivation and brain development.

Heterotrimeric G protein Gα$_q$ is required for NSC reactivation

It is well known that GPCR/G protein signaling regulates actin dynamics to control many cellular processes, such as morphogenesis, cell motility, and axonal development (*39*). Since mouse Gα$_q$ regulates neuronal migration during early brain development (*40*), we assessed the role of GPCR/Gα$_q$ protein signaling in qNSC reactivation. We found that Gα$_q$ KD resulted in defects in qNSC reactivation (fig. S3, A to C). qNSCs in larval brains carrying loss-of-function alleles of *G*α$_q$ (*G*α$_q^{221C}$) and a hemizygous *G*α$_q^{221C/Df(2R)Gαq1.3}$ mutant had a delayed reactivation [36.9% EdU-negative NSCs in *G*α$_q^{221C}$ and 36.8% EdU-negative NSCs in *G*α$_q^{221C/Df(2R)Gαq1.3}$] compared to control (14.9% EdU-negative NSCs) at 24-hour ALH (Fig. 3, A and C, and fig. S3, D and E). In addition, more NSCs retained primary protrusions in *G*α$_q^{221C}$-mutant larval brains than in the control (Fig. 3, A and D). However, knocking down *G*α$_q$ in glial cells or fat body did not cause any reactivation defect (fig. S5). These observations suggest that Gα$_q$ is required intrinsically for qNSC reactivation.

Although Dia is known to be required for cytokinesis (*41*), no cytokinesis defects were found in *dia*^{1}-mutant larval brains at 24-hour ALH ($n = 11$), and *dia* KD only exhibited a very mild cytokinesis defect in NSCs (5%, $n = 10$) at 24-hour ALH. Even in *dia*^{5}, the null mutant, only a weak cytokinesis defect [Fig. 2A, white arrows, large multinucleated cells (*42*); 11%, $n = 10$] in NSCs was observed at 24-hour ALH. In addition, *rho1* KD resulted in a negligible cytokinesis phenotype (3%, $n = 11$), while Gα$_q$ KD had no obvious effect on NSC cytokinesis ($n = 15$). Therefore, the cytokinesis defect does not notably contribute to the reactivation phenotypes observed in this study. In addition, *G*α$_q$ and *dia* KD using *grh-GAL4* did not obviously affect larval growth or the pupariation rate.

To investigate whether Gα$_q$ activation is sufficient to promote NSC reactivation upon fed and nutrition restriction, we overexpressed a constitutively active form of Gα$_q$ (Gα$_q^{Q203L}$) under the control of *grh-GAL4*. Gα$_q^{Q203L}$ overexpression triggered an increase in the number of NSCs reentering the cell cycle (Fig. 3, E and F; control, 20.5% EdU-positive NSCs; Gα$_q^{Q203L}$, 33.8%) only under fed condition but not under nutrition restriction condition (fig. S6).

Small GTPase Rho1 is required for NSC reactivation

Small GTPase Rho1/RhoA is a known activator of Dia/Formin (*43*) and a downstream effector of Gα$_q$ signaling that controls F-actin remodeling in fibroblast (NIH 3TC) and HEK293 cells (*30*, *44*–*46*). Therefore, we investigated the function of *Drosophila* Rho1 in qNSC reactivation. Since loss-of-function alleles of *Rho1* causes embryonic lethality, we analyzed the effect of Rho1 KD in the larval brain. In two independent *rho1* RNAi strains under the control of *grh*-Gal4, the percentage of NSCs without EdU incorporation was substantially increased from 8.9% in the control NSCs to 28.7 and 32.5% in *rho1*$^{RNAi-1}$ [Bloomington Drosophila Stock Center (BDSC), #9909]– and *rho1*$^{RNAi-2}$ (BDSC, #9910)–expressing NSCs, respectively, at 24-hour ALH (Fig. 3, B and C). Likewise, overexpression of a dominant-negative form of Rho1 (Rho1^{N19}), driven by *grh-GAL4,* resulted in an increased percentage of EdU-negative NSCs (25.8%) at 24-hour ALH (Fig. 3, B and C). In addition, more NSCs retained primary protrusions in *rho1*$^{RNAi-1}$-, *rho1*$^{RNAi-2}$-, or *Rho1*^{N19}-expressing NSCs (Fig. 3, B and D). These data established an intrinsic role for Rho1 in qNSC reactivation. Similar to Gα$_q^{Q203L}$ overexpression, overexpression of GFP-Rho1 in NSCs resulted in a significant increase in the number of reactivated NSCs (Fig. 3, E and F) under fed condition. Our observations suggest that Rho1 is required for NSC cell cycle reentry in the presence of nutrition.

Gα$_q$ promotes qNSC reactivation through Rho1 activation

To assess the cellular pattern of active Rho1 in qNSCs, we took advantage of Dia-Rho1–binding domain (DiaRBD)–GFP, which binds specifically to active Rho1 (*47*), and overexpressed it in the NSCs using *grh-GAL4* driver. DiaRBD-GFP was found in both the soma and primary protrusions of control qNSCs at 6-hour ALH (Fig. 3, G and H). Notably, Gα$_q$ KD resulted in a specific reduction in DiaRBD-GFP signal in the primary protrusions (Fig. 3, G and H), suggesting Gα$_q$-mediated Rho1 activation in the primary protrusions of qNSCs. Next, we determined whether Gα$_q$ acts upstream of Rho1 during NSC reactivation. GFP-Rho1 overexpression fully suppressed defects in cell cycle reentry caused by Gα$_q$ depletion (Fig. 3, I and J). While there were 20.5% EdU-negative NSCs in *G*α$_q$-KD NSCs (with GFP overexpression as a control) at 24-hour ALH, GFP-Rho1 overexpression reduced the number of qNSCs to 8.5% ($n = 16$) upon *G*α$_q$ depletion, which was indistinguishable from the control group (Fig. 3, H and I; 7.9%, $n = 15$). Meanwhile, the overexpression of GFP-Rho1 alone did not affect cell cycle reentry of qNSCs at 24-hour ALH (Fig. 3, I and J). These results strongly suggest that Gα$_q$ promotes cell cycle reentry of qNSCs through Rho1 activation in the primary protrusion.

Gα$_q$-Rho1 signaling promotes NSC reactivation via Dia-mediated F-actin remodeling

Given that Gα$_q$ is required for Rho1 activation in the primary protrusions of qNSCs (Fig. 3G), we determined whether Gα$_q$ is also required for Dia protein localization in these cells. Using anti-Dia antibodies, we detected Dia in the cytoplasm of soma and primary protrusions of qNSCs (Fig. 4, A and B). Knocking down *G*α$_q$ using two independent RNAi lines markedly reduced Dia levels in the primary protrusions (Fig. 4, A and B). Similarly, Dia localization in the primary protrusion was diminished upon *rho1* depletion in NSCs (Fig. 4, A and B).

Next, we assessed the effects of Gα$_q$, Rho1, and Dia on F-actin remodeling in qNSCs at 6-hour ALH by live-cell imaging of GFP::utABD. F-actin retrograde flow from the primary protrusion to the soma was

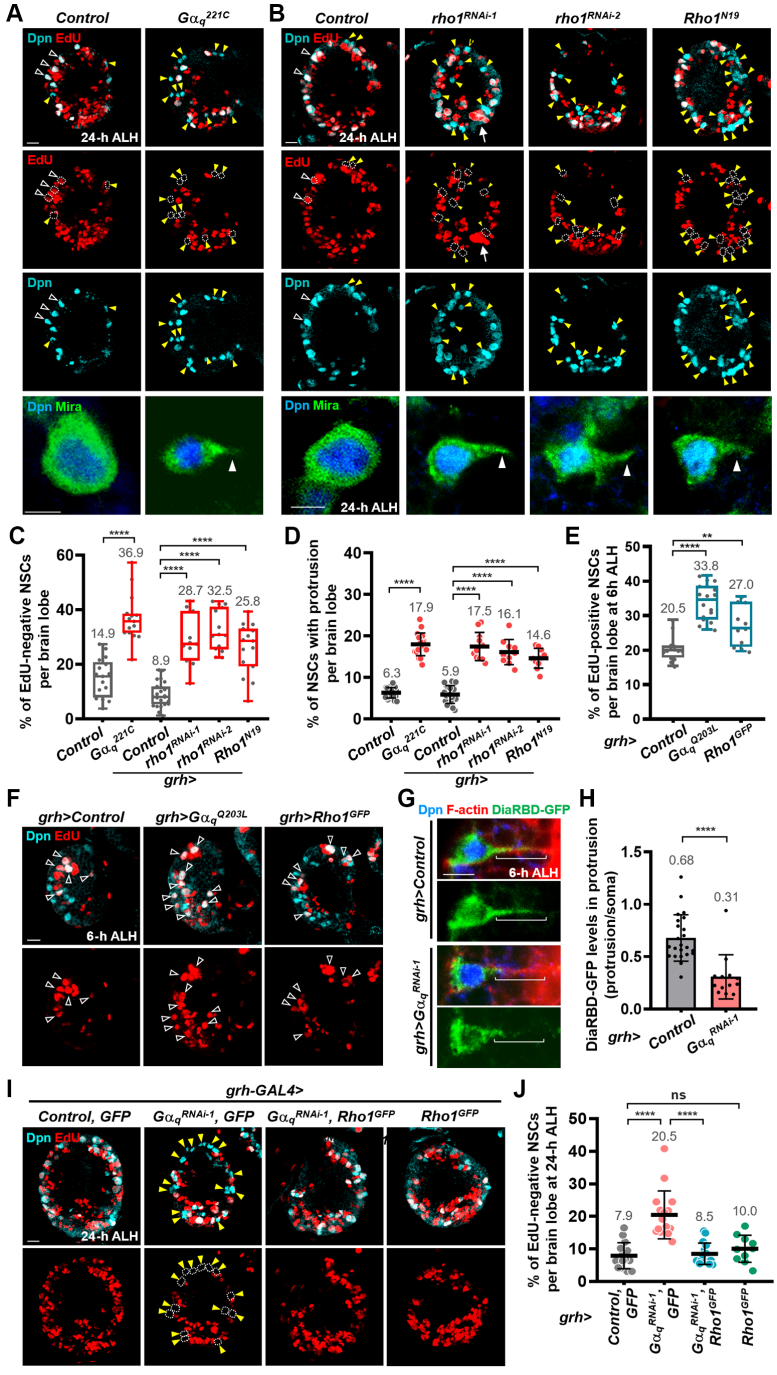

Fig. 3. $G\alpha_q$-Rho1 signaling promotes qNSC reactivation. (**A** and **B**) Larval NSCs were labeled with EdU and Dpn at 24-hour ALH. Yellow arrows and dashed circles, EdU-negative NSCs; white arrows, EdU-positive NSCs. Bottom row: NSCs were labeled with Dpn and Mira. White arrows, protrusion of NSCs; white arrows, NSCs with cytokinesis defects. (**C**) Quantification graph of EdU-negative qNSCs in (A) and (B). *Control (yw)*: 14.9 ± 7.1, $n = 17$; $G\alpha_q^{221C}$: 36.9 ± 8.8, $n = 15$; *Control* (β-*gal*^{RNAi}): 8.9 ± 4.6, $n = 23$; *rho1*$^{RNAi-1}$: 28.7 ± 9.3, $n = 11$; *rho1*$^{RNAi-2}$: 32.5 ± 7.7, $n = 14$; *Rho1*^{N19}: 25.8 ± 9.2, $n = 15$. (**D**) Quantification graph of NSCs retaining protrusion in (A) and (B). *Control (yw)*: 6.3 ± 1.3, $n = 21$; $G\alpha_q^{221C}$: 17.9 ± 2.7, $n = 18$; *Control* (β-*gal*^{RNAi}): 5.9 ± 2.1, $n = 20$; *rho1*$^{RNAi-1}$: 17.5 ± 3.4, $n = 11$; *rho1*$^{RNAi-2}$: 16.1 ± 3.0, $n = 10$; *Rho1*^{N19}: 14.6 ± 2.4, $n = 10$. (**E**) Quantification graph of EdU-positive NSCs at 6-hour ALH. *Control* (β-*galRNAi*): 20.5 ± 3.6, $n = 14$; $G\alpha_q^{Q203L}$: 33.8 ± 5.3, $n = 18$; *Rho1*^{GFP}: 27.0 ± 5.8, $n = 11$. (**F**) Proliferating NSCs (EdU, red; Dpn, cyan) in control (β-*gal*^{RNAi}), $G\alpha_q^{Q203L}$, and *GFP-Rho1* larval brains driven by *grh-GAL4* at 6-hour ALH. White arrows, EdU$^+$ NSCs. (**G**) qNSCs (Dpn, cyan) in control (β-*gal*^{RNAi}) and $G\alpha_q$-KD larval brains under *grh-GAL4* at 6-hour ALH. F-actin (rhodamine phalloidin) marks protrusions. DiaRBD-GFP (green) marks active Rho1. (**H**) Quantification graph of DiaRBD-GFP levels in the protrusion in (G). *Control* (β-*gal*^{RNAi}): 0.68 ± 0.22, $n = 23$; $G\alpha_q^{RNAi-1}$: 0.31 ± 0.21, $n = 13$. (**I**) Proliferating NSCs (EdU, red; Dpn, cyan) in larval brains at 24-hour ALH. UAS-GFP, a negative control for suppression effect. Yellow arrows and dashed circles, EdU-negative NSCs. (**J**) Quantification graph of EdU-negative NSCs in (I). *Control* (β-*gal*^{RNAi}),*GFP*: 7.9 ± 4.0, $n = 15$; $G\alpha_q^{RNAi-1}$, *GFP*: 20.5 ± 7.4, $n = 16$; $G\alpha_q^{RNAi-1}$, *Rho1*^{GFP}: 8.5 ± 3.3, $n = 16$; *Rho1*^{GFP}: 10.0 ± 4.1, $n = 10$. One-way ANOVA (C, D, E, and J) and unpaired Student's *t* test (H) are used for statistics. ***$P < 0.001$; **$P < 0.01$. The means of analyzed phenotypes were showed above each column. Scale bars, 10 μm [A, B (top row), F, and I), 5 μm [A, B (bottom row), and G (bottom row)]. ns, no significance.

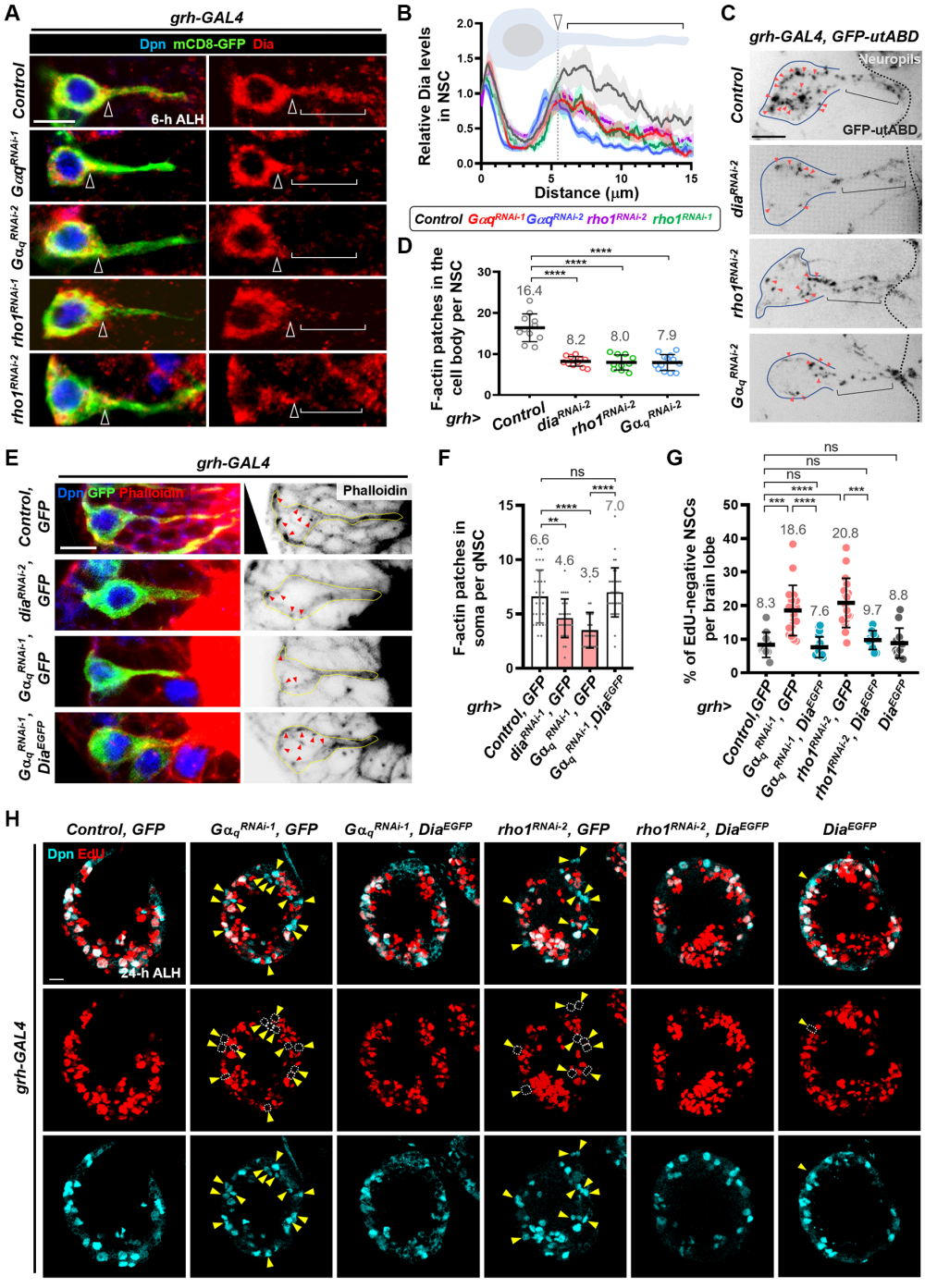

Fig. 4. Gα$_q$-Rho1-Dia signaling promotes NSC reactivation via actin cytoskeleton. (**A**) Dia protein (red) in qNSCs (Dpn, blue; mCD8-GFP, green) in control (β-*gal*^{RNAi}), *Gα$_q$*-KD, and *rho1*-KD larval brains under the control of *grh*-GAL4 driver at 6-hour ALH. Yellow arrows, neck region of qNSC; brackets, primary protrusion. (**B**) Quantification graph of Dia protein levels along the soma and protrusion of qNSC in various RNAi transgenes driven by *grh-GAL4* driver. (**C**) F-actin patches (GFP-utABD, black) in control (β-*gal*^{RNAi}), *Gα$_q$*-KD, *rho1*-KD, and *dia*-KD qNSCs under the control of *grh-GAL4* driver at 6-hour ALH. Solid lines outline the soma of NSCs. Dashed lines indicate the boundary of neuropil. Brackets, primary protrusion. (**D**) Quantification graph of F-actin patches in the soma of qNSCs in various genotypes of (C). *Control* (β-*gal*^{RNAi}): 16.4 ± 3.4, $n = 11$; *dia*$^{RNAi-2}$: 8.2 ± 1.2, $n = 11$; *rho1*$^{RNAi-2}$: 8.0 ± 1.8, $n = 16$; *Gα$_q$*$^{RNAi-2}$: 7.9 ± 1.9, $n = 13$. (**E**) F-actin (rhodamine phalloidin, red and black) in qNSCs (Dpn, blue; mCD8-GFP, green) under *grh-GAL4* driver at 6-hour ALH. Red arrows, F-actin patches. Yellow lines mark intact qNSCs. (**F**) Quantification graph of F-actin patches in the soma of qNSCs in various genotypes of (G). *Control* (β-*gal*^{RNAi}),*GFP*: 6.6 ± 2.4, $n = 29$; *dia*$^{RNAi-1}$, *GFP*: 4.6 ± 1.8, $n = 29$; *Gα$_q$*$^{RNAi-1}$, *GFP*: 3.5 ± 1.6, $n = 25$; *Gα$_q$*$^{RNAi-1}$, *Dia*^{EGFP}: 7.0 ± 22, $n = 34$. (**G**) Quantification graph of EdU-negative qNSCs in various genotypes of (F). *Control* (β-*gal*^{RNAi}),*GFP*: 8.3 ± 3.8, $n = 10$; *Gα$_q$*$^{RNAi-1}$, *GFP*: 18.6 ± 7.5, $n = 18$; *Gα$_q$*$^{RNAi-1}$, *Dia*^{EGFP}: 7.6 ± 3.1, $n = 19$; *rho1*$^{RNAi-1}$,*GFP*: 20.8 ± 7.3, $n = 18$; *rho1*$^{RNAi-1}$, *Dia*^{EGFP}: 9.7 ± 2.8, $n = 10$; *Dia*^{EGFP}: 8.8 ± 4.5, $n = 13$. (**H**) Proliferating NSCs (EdU, red; Dpn, cyan) in larval brains of various transgenes driven by *grh-GAL4* at 24-hour ALH in (G). Yellow arrows and dashed circles point to EdU-negative NSCs. One-way ANOVA is used for statistics. ****$P < 0.0001$; ***$P < 0.001$; **$P < 0.01$. The means of analyzed phenotypes were shown above each column. Scale bars, 10 μm (H) and 5 μm (A, C, and E).

disrupted in the *dia*-, *rho1*-, and $G\alpha_q$-KD qNSCs (fig. S7 and movie S6). In addition, the depletion of these genes resulted in a marked decrease in the number of F-actin patches in the soma of qNSCs (Fig. 4, C and D, and movie S7). These data suggest that the $G\alpha_q$-Rho1-Dia signaling axis regulates the retrograde flow and polymerization of F-actin in the soma of qNSCs.

Next, we performed epistatic analysis to determine whether Dia functions downstream of $G\alpha_q$ to mediate F-actin remodeling and/or NSC reactivation. Dia–enhanced GFP (EGFP) overexpression under *grh*-GAL4 completely suppressed the reduction in F-actin patches and defects in NSC reactivation in $G\alpha_q$-depleted qNSCs (Fig. 4, E to H). Dia-EGFP overexpression alone, in the absence of $G\alpha_q$ depletion, did not affect the reactivation (Fig. 4, G and H). Likewise, Dia-EGFP overexpression suppressed *rho1* KD–induced defects in NSC cell cycle reentry (Fig. 4, G and H). Our results suggest that the $G\alpha_q$-Rho1 signaling axis promotes NSC reactivation via Dia-mediated F-actin remodeling.

F-actin polymerization is required for the reactivation of qNSCs

Since Dia promotes F-actin polymerization and NSC reactivation, we determined whether F-actin polymerization is important for qNSC reactivation. To address this, we examined the potential roles of two groups of F-actin polymerization regulators, the positive regulators Profilin [*chickadee* (*chic)* in *Drosophila*], *spire* (*spir)*, and *singed* (*sn*) and the negative regulators Cofilin [*twinstar* (*tsr)* in *Drosophila*], *capping protein beta* (*cpb*), and *capulet* (*capt*). A reduction in F-actin polymerization via knocking down positive regulators or overexpressing negative regulators results in defective NSC reactivation (fig. S8A). In contrast, when F-actin polymerization was enhanced by the depletion of negative regulators or overexpression of positive regulators, qNSCs reactivation was unaltered (fig. S8B). Knocking down Arp2, Arp3, or WASp, regulators for F-actin branching, in NSCs did not cause NSC reactivation defect (fig. S8C), suggesting that branched F-actin is not important for NSC reactivation. These findings strongly indicate that F-actin polymerization is required for NSC reactivation.

The Hippo-Warts-Yorkie signaling pathway is not a functional target of Dia in NSC reactivation

To understand how F-actin remodeling influence NSC reactivation, we assessed whether Dia could control NSC reactivation via regulating Yorkie (Yki) activity in qNSCs. Some earlier studies have suggested that Yki activity, which is controlled by the evolutionarily conserved Hippo signaling pathway and which can respond to biomechanical cues such as tension within the F-actin cytoskeleton in various cell types (*48*, *49*), is necessary for qNSC reactivation (*18*, *19*). Nuclear Yki levels were notably reduced in dia^1- and dia^5-mutant qNSCs (fig. S9, A and B). Similarly, RNAi-induced *dia* KD reduced nuclear Yki levels in the NSCs (fig. S9, C and D). However, neither overexpression of a constitutively active form of Yki (Yki^{S168A}-GFP) nor knocking down *Warts* (*Wts*) that phosphorylates and inactivates Yki could suppresses NSC reactivation defects in the *dia*-depleted larval brains (fig. S9, E and F). These observations suggest that the reduction of nuclear Yki might be a consequence, but not the cause of delayed reactivation upon *dia* depletion, and that the Hippo-Wts-Yki signaling pathway is unlikely to be a functional target of Dia during NSC reactivation.

Transcription factors Mrtf and serum response fibroblast are required for NSC reactivation

Formin-mediated F-actin assembly triggers the nuclear translocation of the conserved MRTF and activates MRTF/serum response factor (SRF) signaling in mammalian smooth muscle cells and embryonic fibroblasts (*50*–*53*). *Drosophila* Mrtf is known to regulate tracheal branching and cell migration (*54*, *55*), but its potential function during brain development is not established. Thus, we examined the function of Mrtf and Blistered (Bs; *Drosophila* homolog of SRF) in NSC quiescence exit. NSC reactivation was impaired in both *mrtf* and *bs* mutants; qNSCs in larval brains carrying loss-of-function alleles of $Mrtf^{\Delta 7}$ and a hemizygous $Mrtf^{\Delta 7/Df(3L)BSC412}$ showed delayed reactivation [51.4% EdU-negative NSCs in $Mrtf^{\Delta 7}$ larvae and 45.1% EdU-negative NSCs in $Mrtf^{\Delta 7/Df(3L)BSC412}$ larvae] compared with control (17.9% EdU-negative NSCs) at 24-hour ALH (Fig. 5, A and C). Similarly, *mrtf* KD in NSCs led to delayed reactivation, seen by an increase in the percentage of EdU-negative NSCs from 9.8% in the control to 20.2 and 29% in the $mrtf^{RNAi\text{-}1}$- and $mrtf^{RNAi\text{-}2}$-expressing NSCs, respectively, at 24-hour ALH (Fig. 5, B and C). The findings suggested that *mrtf* is intrinsically required for NSC reactivation. In addition, larval brains carrying loss-of-function alleles of $bs^{\Delta 0326}$ and a hemizygous $bs^{03267/Df(2R)Exel6082}$ showed delayed NSC reactivation [29.6% EdU-negative NSCs in $bs^{\Delta 0326}$ and 38.1% EdU-negative NSCs in $bs^{03267/Df(2R)Exel6082}$ larvae] compared with control NSCs (17.9% EdU-negative NSCs) at 24-hour ALH (fig. S10, A and B). These data suggest that SRF-Mrtf signaling promotes qNSC reactivation.

Nuclear Mrtf localization correlates with the active state of NSCs

To assess the localization pattern of Mrtf in NSCs, we expressed GFP-tagged Mrtf, Mrtf-3×GFP [driven by ubiquitous *tubulin* (*tub*) promoter]—a functional form that can fully rescue the ovarian defect seen in the loss-of-function allele of $mrtf^{\Delta 7}$ (*56*). Notably, nuclear Mrtf-GFP intensity was higher in both mushroom body NSCs at 0-hour ALH and central brain NSCs at 24-hour ALH when compared with nonmushroom body NSCs at 0-hour ALH (fig. S10, C to I), suggesting that nuclear Mrtf correlates with the active status of NSCs.

To examine the localization of endogenous Mrtf in NSCs, we generated polyclonal anti-Mrtf antibodies against C-terminal *Drosophila* Mrtf (1119 to 1418 amino acids encoded in exon 5). Endogenous Mrtf was localized in both the cytoplasm and nucleus in control NSCs (Fig. 5, D and E), similar to GFP-tagged Mrtf (fig. S10, C to H). The nuclear intensity and the nucleocytoplasmic ratio of Mrtf were decreased in $Mrtf^{\Delta 7}$-mutant NSCs at 24-hour ALH (Fig. 5, D and E). In addition, total Mrtf protein was reduced in $Mrtf^{\Delta 7}$- and $Mrtf^{KO}$-mutant brains, in which exon 1 and exons 4 to 5 were deleted, respectively (fig. S10, J and K), suggesting the specificity of the antibody.

The $G\alpha_q$-Rho1-Dia pathway promotes NSC reactivation through the transcription factor Mrtf

We wondered whether Dia would be important for the nuclear localization of Mrtf in NSCs via F-actin polymerization. The nuclear intensity and nucleocytoplasmic ratio of Mrtf were decreased in dia^5-mutant NSCs (Fig. 5, D and E), as well as in $G\alpha_q^{221C}$-mutant, *rho1*-KD, and $Rho1^{N19}$-overexpressing NSCs at 24-hour ALH

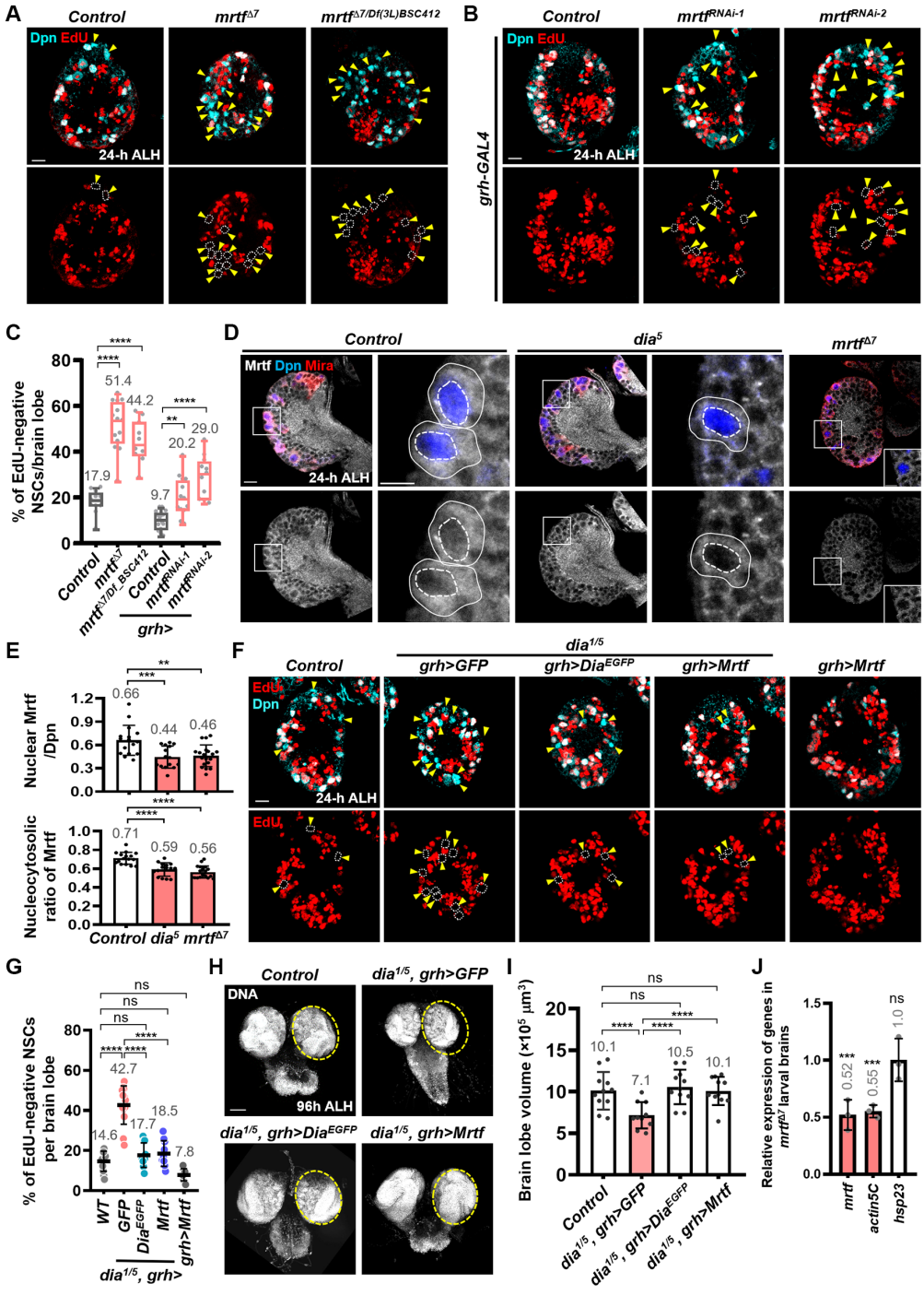

Fig. 5. Dia promotes qNSC reactivation and brain development via transcription factor Mrtf. (**A** and **B**) Larval NSCs were labeled with EdU and Dpn at 24-hour ALH. Yellow arrows and dashed circles, EdU-negative NSCs. (**C**) Quantification graph of EdU-negative NSCs in (A) and (B). *Control(yw)*: 17.9 ± 5.2, $n = 11$; $mrtf^{D7}$: 51.4 ± 10.7, $n = 14$; $mrtf^{D7/Df(3L)BSC412}$: 44.2 ± 9.2, $n = 10$; *Control* (β-gal^{RNAi}): 9.7 ± 4.1, $n = 15$; $mrtf^{RNAi-1}$: 20.2 ± 8.7, $n = 13$; $mrtf^{RNAi-2}$: 29.0 ± 9.0, $n = 11$. (**D**) NSCs were labeled with Mrtf, Dpn, and Mira. White squares, the region for high magnification. Solid lines, NSCs. Dashed circles, nucleus. (**E**) Quantification graph of nuclear Mrtf expression (top) and ratio of nuclear Mrtf to cytoplasmic Mrtf (bottom). Top graph: *Control (yw)*: 0.66 ± 0.2, $n = 16$; dia^5: 0.44 ± 0.14, $n = 15$; $mrtf^{D7}$: 0.46 ± 0.14, $n = 16$. Bottom graph: *Control (yw)*: 0.71 ± 0.06, $n = 16$; dia^5: 0.59 ± 0.07, $n = 15$; $mrtf^{D7}$: 0.56 ± 0.06, $n = 19$. (**F**) Larval NSCs were labeled with EdU and Dpn at 24-hour ALH. Yellow arrows and dashed circles, EdU-negative NSCs. (**G**) Quantification graph of EdU-negative NSCs in (E). *Control (yw)*: 14.6 ± 5.0, $n = 11$; $dia^{1/5}$, *grh>GFP*: 42.7 ± 9.6, $n = 13$; $dia^{1/5}$, $grh>Dia^{EGFP}$: 17.7 ± 6.1, $n = 10$; $dia^{1/5}$, *grh>Mrtf*: 18.5 ± 6.4, $n = 10$; *grh>Mrtf*: 7.8 3.0, $n = 10$. (**H**) The size of larval brains (DNA, gray) at 96-hour ALH. Dashed circles, single brain lobe. (**I**) Quantification graph of brain size from *Control (yw)*: 10.1 ± 2.3, $n = 11$; $dia^{1/5}$, *grh>GFP*: 7.1 ± 1.6, $n = 10$; $dia^{1/5}$, $grh>Dia^{EGFP}$: 10.6 ± 2.1, $n = 11$; $dia^{1/5}$, *grh>Mrtf*: 10.1 ± 1.7, $n = 11$. (**J**) Quantification graph of reverse transcription quantitative polymerase chain reaction (RT-qPCR) analysis in 24-hour ALH brains from control (*yw*) and $mrtf^{\Delta 7}$. After normalization against *yw* control (with SD): *mrtf*, 0.52 ± 0.08–fold; *actin5C*, 0.55 ± 0.03–fold; *Hsp23*, 1.00 ± 0.11–fold. One-way ANOVA is used for statistics. ***$P < 0.001$. The means of analyzed phenotypes were shown above each column. ***$P < 0.001$; **$P < 0.01$. The means of analyzed phenotypes were shown above each column. Scale bars, 50 μm (H), 10 μm (A, B, D, and F), and 5 μm (D) (for images with high magnification).

(fig. S11, A to D). Next, we assessed whether Mrtf overexpression could suppress the *dia*-mutant phenotypes. Mrtf overexpression completely suppressed defects in EdU incorporation in the transheterozygous *dia* mutant ($dia^{1/5}$) (Fig. 5, F and G), while overexpression of Mrtf alone did not affect NSC reactivation (Fig. 5, F and G). Likewise, Mrtf overexpression suppressed defects in EdU incorporation in $G\alpha_q$-KD and *rho1*-KD NSCs (fig. S11, E and F). These results indicate that Mrtf acts downstream of the $G\alpha_q$-Rho1-Dia pathway to promote qNSC reactivation.

Similar to DIAPH1, variants in MRTF have been identified in human patients with microcephaly (*23*, *24*, *57*, *58*). We found that overexpression of Mrtf in the NSCs reversed the microcephaly-like phenotype seen in the transheterozygous $dia^{1/5}$ mutant to the control brain volume (Fig. 5, H and I), further supporting that Mrtf functions downstream of Dia-mediated F-actin remodeling in the NSCs during brain development.

Since actin is a known transcriptional target of Mrtf in *Drosophila* ovary and breast cancer cells (*56*), we tested whether Mrtf could regulate *actin* in the larval brain. *actin5C* expression was substantially reduced in $mrtf^{\Delta 7}$-mutant brains (Fig. 5J), suggesting a positive feedback regulation between Mrtf and actin that leads to enhanced *actin* expression and Mrtf nuclear localization during qNSC reactivation.

GPCR Smog promotes qNSC reactivation via the $G\alpha_q$-Dia pathway

To identify the GPCR that activates $G\alpha_q$ in the NSCs, we examined the expression of a total of 123 GPCRs from the published single-cell RNA sequencing (scRNA-seq) database of the *Drosophila* larval brain (*59*). From this dataset, we identified 36 GPCRs that were expressed in NSCs (fig. S12, A to C). Next, we performed a small-scale RNAi screen, and 5 of 36 GPCRs showed potential defects in NSC reactivation. Among these five candidates, we found that a GPCR named Smog, a protein interacting with $G\alpha_q$ in the mouse brain (*60*), is required for qNSC reactivation (Fig. 6, A and B). At 24-hour ALH, two independent *smog* RNAi lines displayed defects in NSC reactivation with a significant increase in EdU-negative NSCs [20.5% in $smog^{RNAi\text{-}2}$ (BDSC, #43135) and 25.1% in $smog^{RNAi\text{-}2}$ (BDSC, #51705)] compared to control NSCs (7.9%) (Fig. 6, A and B). qNSCs in larval brains carrying a loss-of-function allele *smog knockout* ($smog^{KO}$) and a hemizygous mutant $smog^{KO/Df(2L)Exel9062}$ showed delayed NSC reactivation [41.6% EdU-negative NSCs in $smog^{KO}$ larvae and 33.9% EdU-negative NSCs in $smog^{KO/Df(2L)Exel9062}$ larvae compared to 16.7% EdU-negative NSCs in the control larvae] at 24-hour ALH (Fig. 6, C and D). *smog* expression indicated by mouse CD8 (mCD8)–GFP (under the control of *smog*-GAL4) was notably higher in qNSCs than in active NSCs, supporting a role for Smog in the reactivation (fig. S12, D and E). We examined the subcellular localization of Smog in qNSCs using GFP-tagged Smog driven by *spaghetti squash* (*sqh)* promoter (*61*) and found it to be enriched in the primary protrusion of these cells (Fig. 6, E and F). Moreover, knocking down *smog* in qNSCs in both $smog^{RNAi\text{-}1}$ and $smog^{RNAi\text{-}2}$ notably reduced Dia protein levels in the primary protrusion (Fig. 6, G and H), similar to $G\alpha_q$ or *Rho1* depletion (Fig. 4, A and B).

To investigate whether $G\alpha_q$ and Dia act downstream of GPCR Smog to promote NSC reactivation, we overexpressed Dia^{EGFP} or wild-type $G\alpha_q$ ($G\alpha_q^{WT}$), in the *smog*-KD NSCs. Overexpression of Dia^{EGFP} or $G\alpha_q^{WT}$ in the *smog*-KD NSCs significantly suppressed the defect of EdU incorporation in NSCs (Fig. 6, I and J). Overexpressing $G\alpha_q^{WT}$ alone did not affect the reactivation of qNSCs (Fig. 6, I and J). These data suggest that GPCR Smog promotes qNSC reactivation via the $G\alpha_q$-Dia axis.

Astrocytes secrete Fog to promote qNSC reactivation

Fog is a known ligand for the GPCR Smog in *Drosophila* mesoderm, salivary gland, and S2 cells (*61*, *62*). Fog-Smog signaling controls Rho1 activity for epithelial tube formation during salivary gland invagination in the fly (*62*). However, the role of Fog during qNSC reactivation is unknown. We sought to identify the cell type in the larval brain that secretes the Fog protein. We took advantage of a dataset of scRNA-seq published by Avalos *et al.* (*59*) and analyzed *fog* expression in different cell types of the larval brain. Unexpectedly, *fog* was primarily expressed in the glial cells (Fig. 7A), but not in NSCs or neurons. Only a small proportion (~20%) of glial cells had *fog* expression (Fig. 7A). This prompted us to pinpoint the subtype of glial cells that expresses *fog*. There are four subtypes of glial cells in the *Drosophila* central brain, including surface glia (perineurial glia and subperineurial glia), cortex glia, ensheathing glia, and astrocytes (*63*). Our analysis on the same scRNA-seq dataset revealed that *fog* is predominantly expressed in the astrocytes and, to much lesser levels, in the ensheathing glia, but not in the surface glia or cortex glia (Fig. 7B). These analyses pointed out the astrocytes as the main glial cells secreting the Fog protein in the *Drosophila* larval brain.

We next examined whether Fog plays a role in qNSC reactivation. We knocked down *fog* in glial cells using a pan-glia driver (*repo-GAL4*) and found that the down-regulation of Fog in glia caused delayed reactivation of qNSCs (Fig. 7, D and F). By contrast, *fog* KD in the NSCs (by *grh*-GAL4 driver) did not affect the reactivation (fig. S13, A and B). To pinpoint the subtype of glial cells in which Fog mediates qNSC reactivation, various subtype glial cell drivers were used to specifically knock down *fog* and express mCD8-GFP to label these glial cells: *NP6293-GAL4* and *NP2276-GAL4* drivers for perineurial glia and subperineurial glia, respectively; *nrv2-GAL4* driver for cortex glia and ensheathing glia (fig. S13C), while *alrm-GAL4* with mCD8-GFP specifically decorated astrocytes (Fig. 7C). *fog* KD in astrocytes (Fig. 7, E and F; *alrm-GAL4* driver), but not in other glial types (fig. S13, B and D to F), resulted in defective NSC reactivation. We further marked astrocytes by *alrm>GFP* and nuclear Prospero (Pros). As expected, Fog protein levels in the cell body of astrocytes were reduced and increased upon the KD and overexpression, respectively, suggesting an efficient KD and Fog antibody specificity (Fig. 7J and figs. S14 and S15). Fog signal intensity was not obviously altered in the neuropil that contains processes of astrocytes (Fig. 7, I and J, and fig. S14). Perhaps, Fog is more stable or relatively resistant to RNAi in these processes, or the Fog signal in the neuropil was nonspecific.

Recently, Fog protein has been observed in the sensory neurons and BBB glia of embryonic central nervous system and at third instar larval brain (*64*), which was inconsistent with its expression pattern in early larval brains. Unexpectedly, Fog protein intensity in the entire central brain region including presumptive BBB glia was reduced upon astrocyte-specific Fog KD at 24-hour ALH (Fig. 7, H and J, asterisks; and fig. S14). Therefore, astrocytes appear to be the major source of Fog in the early larval brain, and Fog protein detected in the central brain including BBB glia may be derived from astrocytes.

Fog protein levels in astrocytes remain similar throughout early brain development (fig. S16). Moreover, Fog protein levels were not

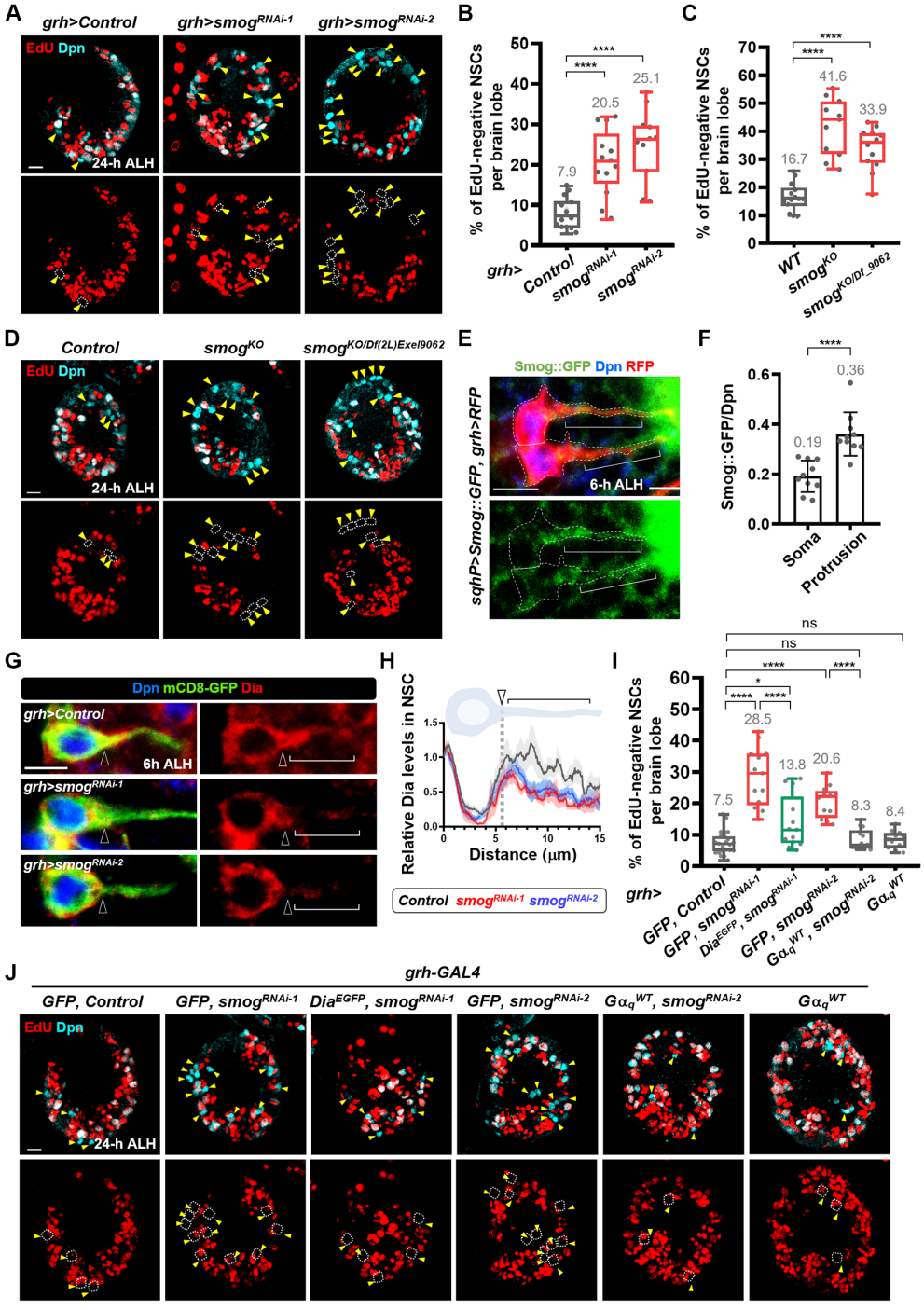

Fig. 6. GPCR Smog promotes qNSC reactivation via $G\alpha_q$-Dia signaling. (**A**) Proliferating NSCs (EdU, red; Dpn, cyan) in control (β-gal^{RNAi}) and *smog*-KD larval brains under the control of *grh-GAL4* driver at 24-hour ALH. Yellow arrows and dashed circles point to EdU-negative NSCs. (**B**) Quantification graph of EdU-negative NSCs of A at 24-hour ALH. *Control* (β-gal^{RNAi}): 7.9 ± 3.8, $n = 14$; $smog^{RNAi-1}$: 20.5 ± 8.1, $n = 13$; $smog^{RNAi-2}$: 25.1 ± 8.7, $n = 11$. (**C**) Quantification graph of EdU-negative NSCs in control (*yw*)– and *smog*-mutant flies in (D). *Control (yw)*: 16.7 ± 4.9, $n = 14$; $smog^{KO}$: 41.6 ± 10.0, $n = 11$; $smog^{KO/Df(2L)Exel9062}$: 33.9 ± 7.6, $n = 12$. (**D**) Proliferating NSCs (EdU, red; Dpn, cyan) in larval brains at 24-hour ALH. (**E**) Smog::GFP localization (green) in the qNSCs [Dpn, blue; red fluorescent protein (RFP); red] in the larval brains at 6-hour ALH. Dashed lines, intact qNSCs; brackets, primary protrusions. (**F**) Quantification graph of Smog::GFP levels in the soma and protrusion of qNSCs. Soma: 0.19 ± 0.06, $n = 10$; protrusion: 0.36 ± 0.09, $n = 10$. (**G**) Dia protein (red) in control (β-gal^{RNAi}) and *smog*-KD qNSCs (Dpn, blue; mCD8-GFP, green) under the control of *grh-GAL4* driver at 6-hour ALH. (**H**) Quantification graph of Dia protein levels along the soma and protrusion in control (β-gal^{RNAi}) and *smog*-KD qNSCs at 6-hour ALH in (G). (**I**) Quantification graph of EdU-negative NSCs in J. *Control* (β-gal^{RNAi}), *GFP*: 7.5 ± 3.7, $n = 23$; $smog^{RNAi-1}$, *GFP*: 28.5 ± 9.2, $n = 13$; $smog^{RNAi-1}$, Dia^{EGFP}: 13.8 ± 8.3, $n = 13$; $smog^{RNAi-2}$, *GFP*: 20.6 ± 5.1, $n = 12$; $smog^{RNAi-2}$, $G\alpha_q^{WT}$: 8.3 ± 3.3, $n = 13$ $G\alpha_q^{WT}$: 8.4 ± 2.8, $n = 11$. (**J**) Proliferating NSCs (EdU, red; Dpn, cyan) in larval brains at 24-hour ALH. Yellow arrows and dashed circles, EdU-negative NSCs. One-way ANOVA (B, C, and L) and unpaired Student's *t* test (F and H) were used for statistics. ****$P < 0.0001$; *$P < 0.05$. The means of analyzed phenotypes were shown above each column. Scale bars, 10 μm (A, D, and J) and 5 μm (E and G).

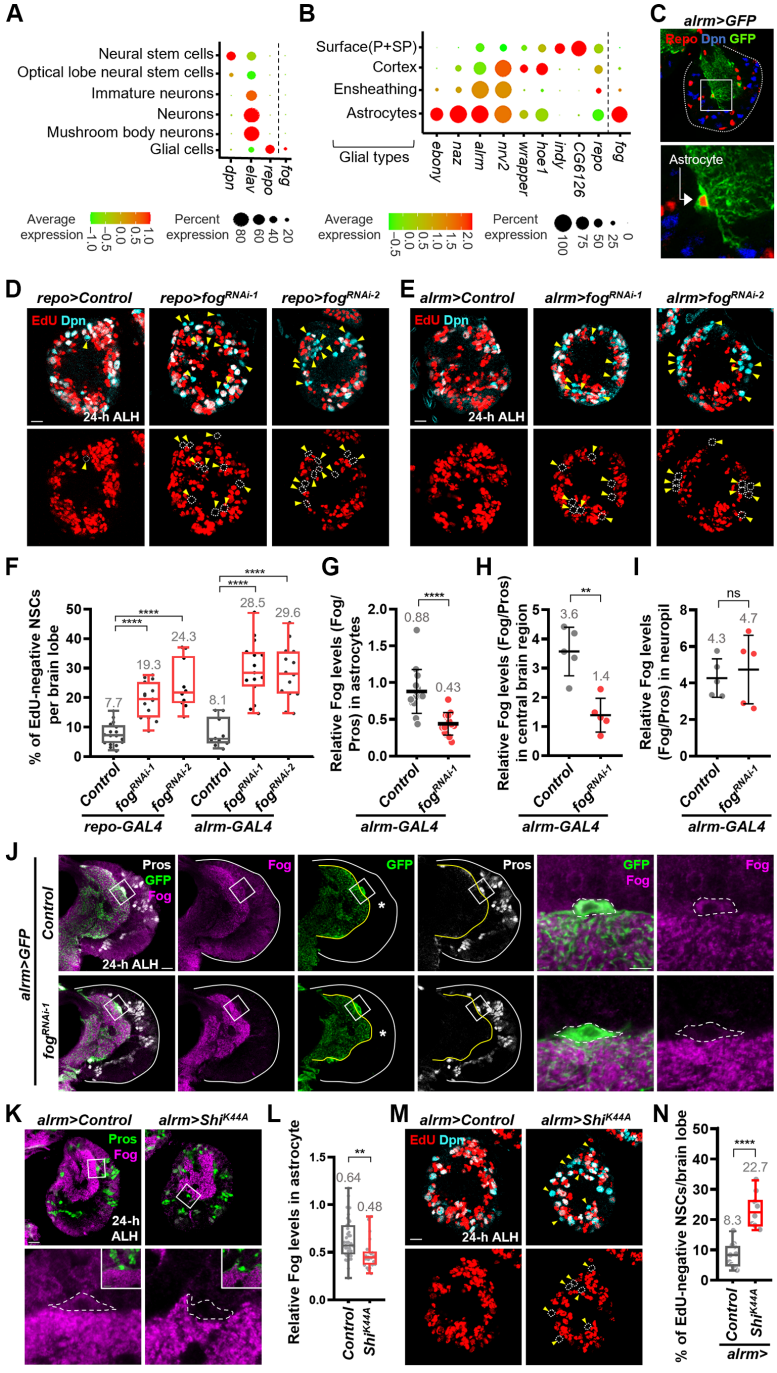

Fig. 7. Astrocytes, a new NSC niche, secrete Fog via dynamin to promote qNSC reactivation. (**A** and **B**) *fog* mRNA expression in larval brains from the dataset of scRNA-seq (refer to Materials and Methods). (**C**) Astrocyte (Repo and *alrm>GFP*) in larval brain at 24-hour ALH. (**D** and **E**) Larval NSCs (EdU and Dpn) at 24-hour ALH. Yellow arrows and dashed circles, EdU-negative NSCs. (**F**) Quantification graph of EdU-negative NSCs in (C) and (D). *repo>control*: 7.7 ± 3.8, $n = 17$; *repo>fog*$^{RNAi-1}$: 19.3 ± 5.8, $n = 15$; *repo>fog*$^{RNAi-2}$: 24.3 ± 8.4, $n = 10$; *alrm>control*: 8.1 ± 4.8, $n = 10$; *alrm>fog*$^{RNAi-1}$: 28.5 ± 9.1, $n = 14$; *alrm>fog*$^{RNAi-2}$: 29.6 ± 9.6, $n = 15$. (**G**) Quantification graph of Fog levels in astrocytes: control, 0.88 ± 0.29, $n = 15$; *alrm>fog*$^{RNAi-1}$, 0.43 ± 0.15, $n = 14$. (**H**) Fog levels in central brain region: control, 3.57 ± 0.83, $n = 5$; *alrm>fog*$^{RNAi-1}$, 1.39 ± 0.58, $n = 5$. (**I**) Fog levels in neuropil region: control, 4.27 ± 1.05, $n = 5$; *alrm>fog*$^{RNAi-1}$, 4.73 ± 1.87, $n = 5$. (**J**) Larval brains were labeled with Fog, Pros, and GFP at 24-hour ALH. White squares, images with higher magnification on the right; white lines, brain lobe outlines; yellow lines, neuropil outlines; asterisks, central brain regions; dashed outlines, astrocytes. (**K**) Larval brains were labeled with Fog and Pros at 24-hour ALH. (**L**) Quantification graph of Fog levels in astrocytes in *control*: 0.64 ± 0.20, $n = 43$; *alrm>Shi*^{K44A}: 0.48 ± 0.16, $n = 22$. (**M**) Larval NSCs (EdU and Dpn) at 24-hour ALH. (**N**) Quantification graph of EdU-negative NSCs in (M). *alrm>control*: 8.3 ± 4, $n = 12$; *alrm>Shi*^{K44A}: 22.7 ± 5.5, $n = 10$. Yellow arrows and dashed circles, EdU-negative NSCs. One-way ANOVA (F) and two-tailed unpaired Student's *t* test (G, H, I, L, and N) are used for statistics. ****$P < 0.0001$; **$P < 0.01$. The means of analyzed phenotypes were shown above each column. Scale bars, 10 μm (D, E, J, K, and M) and 5 μm (J) (for images with high magnification).

affected by nutritional deprivation (fig. S16). Therefore, the astrocyte niche appears to be unaffected by the nutritional condition, unlike the known BBB glia niche (*5*).

Fog is known to localize to vesicles derived through dynamin-mediated endocytosis before its secretion in the *Drosophila* embryos (*65*). To determine whether astrocytes reactivate qNSCs through dynamin-mediated Fog secretion, we blocked dynamin-mediated endocytosis by overexpressing a dominant negative form of *shibire* K44A (*Shi*^{K44A}) in astrocytes using the *alrm-GAL4* driver. Shi^{K44A} overexpression in astrocytes resulted in defective NSC reactivation at 24-hour ALH (Fig. 7, M and N), suggesting that astrocytes regulate NSC reactivation via dynamin-mediated Fog secretion. Shi^{K44A} overexpression in the astrocytes notably reduced Fog levels in the cell body of astrocytes of the larval brain (Fig. 7, K and L), similar to a previous report on a reduction of Fog protein in the *shibire*$^{[ts1]}$ embryos at the restrictive temperature (*65*). Together, Fog protein is produced by astrocytes and functions specifically in these cells to control the NSC exit from the quiescent state.

Fog promotes qNSC reactivation via Gα$_q$-Rho1-Dia signaling

Next, we tested whether Fog is required for Dia localization in the primary protrusion of qNSCs. Upon Fog KD in astrocytes, Dia protein was notably reduced in the primary protrusion of qNSCs (Fig. 8, A and B). To determine whether Dia is a physiologically relevant target of Fog-mediated GPCR signaling, we first tested whether Dia overexpression in NSCs could suppress NSC reactivation defects induced by astrocytes-specific *fog* KD. Dia overexpression using a combination of *grh*-Gal4 and *alrm*-Gal4 drivers markedly suppressed the NSC reactivation defects caused by *fog* KD (Fig. 8, C and D), while Dia overexpression using *alrm*-Gal4 driver alone did not (Fig. 8, G and H). This observation suggested that Fog secreted from astrocytes promotes NSC reactivation by regulating Dia localization/function. Likewise, NSC reactivation defects induced by *fog* KD were suppressed by overexpression of Gα$_q^{WT}$ or Rho1^{GFP} using a combination of both NSC and astrocyte drivers (Fig. 8, E and F), but not by *alrm -GAL4* driver alone (Fig. 8, G and H). These data indicate that Fog secreted from astrocytes promotes NSC reactivation via Gα$_q$-Rho1-Dia signaling.

DISCUSSION

In this study, we have uncovered fine F-actin structures and a previously uncharacterized retrograde flow of F-actin in qNSCs by ExM-SIM imaging. Our findings suggest that astrocytes function as a new NSC niche that produce the ligand Fog to activate the GPCR Smog-Gα$_q$-Rho1-Dia signaling; this signaling axis induces F-actin retrograde flow and enhances F-actin polymerization in the soma (Fig. 9, A and B), resulting in the nuclear translocation of Mrtf where it associates with its cofactor SRF/Bs and potentially activates target genes essential for NSC reactivation (Fig. 9C). Mrtf is also required for the expression of the *actin5C* gene (Fig. 9C). Therefore, our work establishes the critical role of the Fog-GPCR Smog-Gα$_q$-Rho1-Dia/Formin-MRTF pathway in NSC reactivation.

F-actin dynamics in qNSCs

The primary protrusion of qNSCs is enriched with both microtubules and F-actin filaments (*11*, *16*, *17*). Here, we unravel the structure of these F-actin filaments and characterize their function during qNSC reactivation. We found that F-actin forms filaments and patches in the protrusion of qNSCs, similar to F-actin structures in the axons of cultured mouse hippocampal neurons (*66*, *67*). Unlike F-actin multifilaments formed in the axon shaft (*66*, *67*), most of protrusions in qNSCs contain two twisted F-actin filaments on which F-actin patches move along. While periodic F-actin rings have been found in the axons and dendrites of neurons using STORM super-resolution microscopy (*66*–*68*), the protrusion of qNSCs does not seem to have these ring structures. *N*-methyl-D-aspartate receptor–mediated Ca^{2+} influx reorganizes F-actin from ring structures to fibers in dendrites (*69*). qNSC reactivation is synchronized upon nutrient-dependent calcium oscillations of BBB glia in *Drosophila* larval brains (*70*). Since Gα$_q$/phospholipase C–β signaling is known to control calcium dynamics in neural cells (*71*), it would be interesting to understand whether calcium signaling regulates F-actin dynamics in qNSC protrusions for NSC reactivation. In qNSCs, most of F-actin structures seem to undergo a retrograde flow along F-actin fibers toward the soma. This may redirect F-actin patches from the protrusion back into the soma for future cell growth and division during reactivation. The retrograde F-actin flow during axonal elongation and guidance is known to facilitate neuronal growth cone motility (*72*). The force of F-actin movement is transmitted to extracellular substrates via cell adhesion molecules on the growth cone (*73*). One such cell adhesion molecule (E-cad), which is required for NSC reactivation, was shown to be enriched at the qNSC-neuropil contact sites (*16*). It would be interesting to learn whether E-cad at these sites mediates mechanical tension between qNSCs and the neuropil during reactivation.

Smog/GPR1588-Gα$_q$-Rho1 signaling in brain development and diseases

GPCR signaling regulates a variety of cellular behaviors, including stem cell proliferation and differentiation (*74*, *75*). However, the role of GPCR signaling in NSC's exit from quiescence for reactivation is unknown. We show that the GPCR Smog promotes NSC reactivation via the Gα$_q$-Rho1-Dia pathway. Besides Smog, Mist is another known GPCR for the Fog ligand, and Fog-Mist signaling controls Concertina (Cta; the ortholog of human Gα$_{13}$ in *Drosophila*)–Myosin pathway to remodel actin cytoskeleton for apical constriction during embryogenesis (*76*–*78*). However, knocking down *mist* or *cta* did not cause any NSC reactivation defect (fig. S17). Furthermore, knocking down *Drosophila* γ-aminobutyric acid type B receptor subunit 1 ($GABA_B$-R1) (another GPCR that is highly expressed in NSCs; fig. S12, A to C) did not affect NSC reactivation (fig. S17), although mouse $GABA_B$-R1 is known to couple with Gα$_q$ protein to promote calcium influx in neurons during brain development (*79*). These findings validate the specificity of the Smog-Gα$_q$-Dia pathway in qNSCs.

In mammalian systems, the function of Gpr158 (a homolog of *Drosophila* Smog), GNAQ (Gα$_q$ homolog), and Rho1/RhoA in NSC proliferation during brain development is not established. Mouse *Gpr158* has been shown to control neural functions to promote hippocampal-dependent memory, spatial learning, and mood control (*60*, *80*, *81*). Gpr158 interacts with Gα$_q$ in the hippocampus where NSCs reside (*60*). Further study is needed to understand whether a conserved Gpr158-GNAQ axis regulates NSC proliferation in the mammalian brain. In humans, activating mutations of Gα$_q$ (encoded by the *GNAQ* gene) causes capillary malformations with hyperpigmentation, Sturge-Weber syndrome with brain defects due to hyperproliferation of endothelial cell, and cancers (*82*–*84*). In the

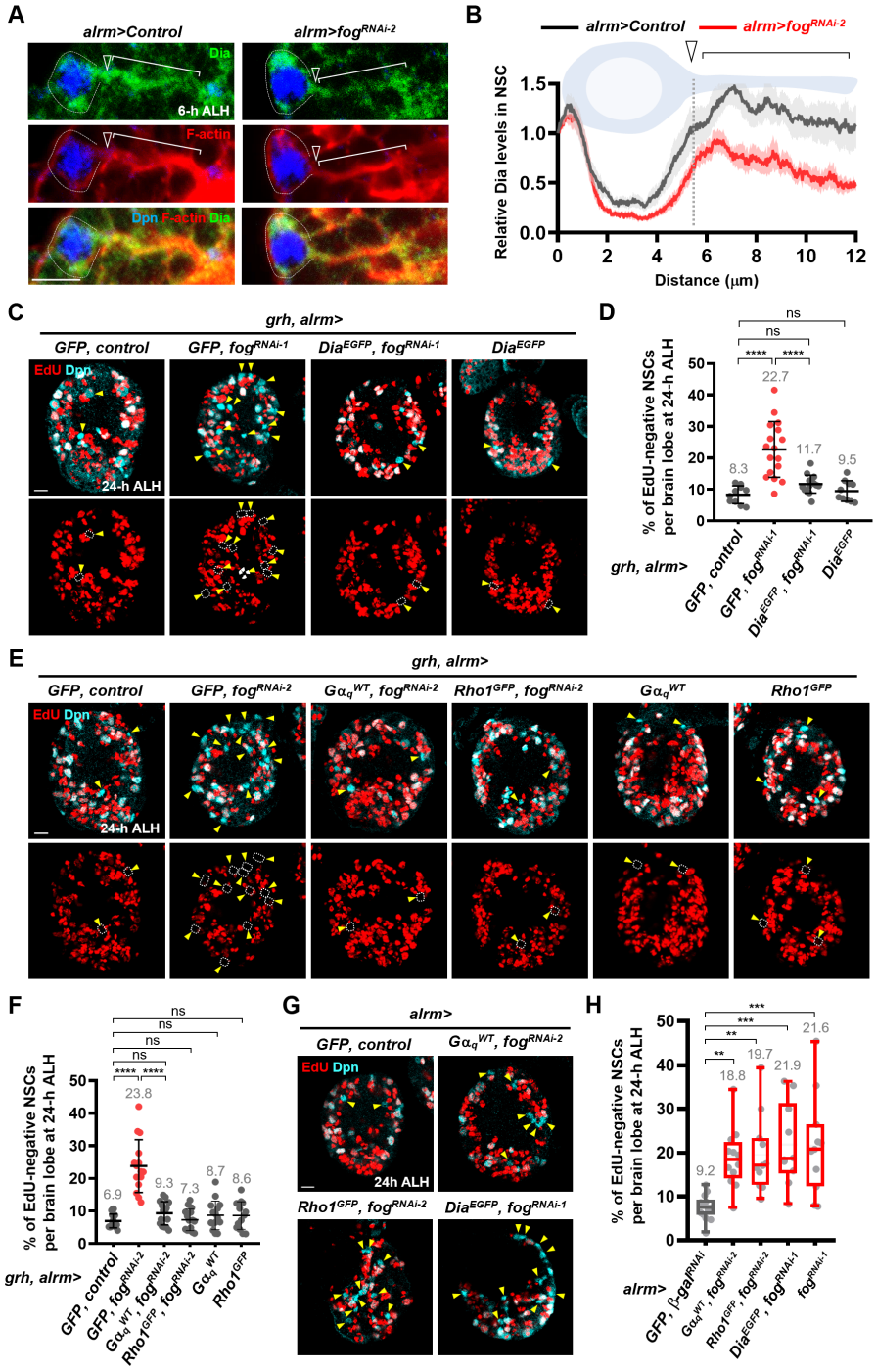

Fig. 8. Niche Fog promotes qNSC reactivation via GPCR Smog-Gα_q-Dia pathway in NSCs. (**A**) qNSCs at 6-hour ALH under the control of *alrm-GAL4* driver were stained for Dia, Dpn, and F-actin. White arrows, neck region of qNSC; brackets, primary protrusion marked by F-actin. (**B**) Quantification graph of Dia levels along the soma and protrusion in qNSCs at 6-hour ALH in control (β-*gal*^{RNAi}) and *fog*-KD in astrocyte-like glia. (**C**) Proliferating NSCs (EdU, red; Dpn, cyan) in various genotypes at 24-hour ALH. (**D**) Quantification graph of EdU-negative NSCs under the control of *grh-GAL4* and *alrm-GAL4* in various genotypes in (C). *Control*: 8.3 ± 2.8, $n = 10$; *GFP, fog*$^{RNAi-1}$: 22.7 ± 8.9, $n = 17$; Dia^{EGFP}, *fog*$^{RNAi-1}$: 11.7 ± 2.8, $n = 15$; Dia^{EGFP}: 9.5 ± 3.3, $n = 10$. (**E**) Proliferating NSCs (EdU, red; Dpn, cyan) at 24-hour ALH. (**F**) Quantification graph of EdU-negative NSCs under the control of *grh-GAL4* and *alrm-GAL4* in various genotypes in (E). *Control*: 6.9 ± 2.1, $n = 18$; *GFP, fog*$^{RNAi-2}$: 23.8 ± 8.1, $n = 15$; Gα_q^{WT}, *fog*$^{RNAi-2}$: 9.3 ± 3.6, $n = 16$; *Rho1*^{GFP}, *fog*$^{RNAi-2}$: 7.3 ± 3.3, $n = 15$. Gα_q^{WT}: 8.7 ± 4.4, $n = 15$; *Rho1*^{GFP}: 8.6 ± 4.3, $n = 13$. (**G**) Proliferating NSCs (EdU, red; Dpn, cyan) in various genotypes at 24-hour ALH. (**H**) Quantification graph of EdU-negative NSCs under the control of *alrm-GAL4* driver in various genotypes in (G). *Control*: 9.2 ± 2.2, $n = 8$; Gα_q^{WT}, *fog*$^{RNAi-2}$: 18.8 ± 6.8, $n = 12$; *Rho1*^{GFP}, *fog*$^{RNAi-2}$: 19.7 ± 8.7, $n = 11$; Dia^{EGFP}, *fog*$^{RNAi-1}$: 21.9 ± 9.3, $n = 10$; *fog*$^{RNAi-1}$: 21.6 ± 11.2, $n = 11$. One-way ANOVA was used for statistics. ****$P < 0.0001$; ***$P < 0.001$; **$P < 0.01$. The means of analyzed phenotypes were showed above each column. Scale bars, 10 μm (C, E, and G) and 5 μm in (A).

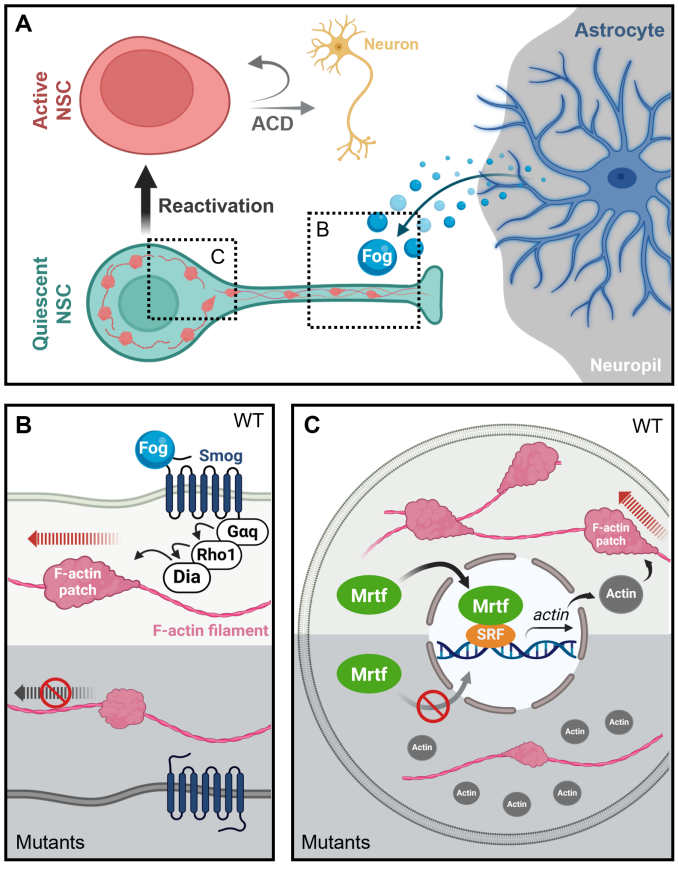

Fig. 9. A working model. (**A**) Fog secreted from astrocytes reactivates qNSCs for asymmetric cell division of NSC to give rise to new neurons. F-actin forms filaments and patches in qNSCs. (**B**) In the primary protrusion of qNSC, GPCR receptor Smog activated by Fog ligand promotes $G\alpha_q$-Rho1-Dia signaling in the protrusion, resulting in the retrograde flow of F-actin patches. In the mutants, active Rho1 and Dia cannot transport to the primary protrusion, resulting the reduction of retrograde flow of F-actin patches, leading to the defect of F-actin dynamics in the soma [please see (C)]. (**C**) In the soma, F-actin patches from primary protrusion promote robust F-actin polymerization and dynamics to consume G-actin, the monomer of actin. Mrtf can translocate to nucleus and promotes *actin* transcription to feedback to F-actin dynamics and the other unknown target genes that are required for cell proliferation. In the mutants, F-actin amount is reduced, probably because of the defect of retrograde flow of F-actin patches in the primary protrusion; therefore, more G-actin monomers may bind to Mrtf and inhibit Mrtf from nuclear translocation.

central nervous system, the GTPase RhoA/Rho1 maintains the integrity of adherens junctions by retaining the organization and number of spinal cord neuroepithelium (NSCs) (*85*). Consistent with this, inactivating variants of human RHOA cause a neuroectodermal syndrome with linear hypopigmentation (*86*, *87*). These reports suggest that $G\alpha_q$-RhoA signaling may have a general role in promoting cell proliferation during development.

Dia-Mrtf signaling regulates NSC proliferation and brain development

Variants of myocardin-like protein 2 (MKL2)/MRTF are associated with neurodevelopmental disorders including microcephaly and autism spectrum disorder (*57*). We found that *Drosophila* $Mrtf^{KO}$, a null mutant, exhibited a microcephaly-like phenotype (fig. S18, A and B). However, the function of mammalian MRTF in NSCs or brain development was unknown. Here, we provide strong evidence that Mrtf is a novel intrinsic factor mediating the exit of *Drosophila* NSCs from quiescence. It will be of great interest to understand whether mammalian Mrtf also regulates NSC proliferation. Consistent with the role of *Drosophila* Dia in NSC reactivation, mammalian Formin 2 activates the Wnt signaling–β-catenin pathway to regulate NSC proliferation during brain development (*88*). Variants of Formins also have been identified in human patients with microcephaly (*23*, *24*, *38*). MRTF is a downstream effector of Formin/Dia-mediated actin dynamics for regulating the transcription of cell motility– and proliferation-related genes in tumor cells and fibroblasts (*89*–*91*). We found that microcephaly-like phenotype in the larva carrying loss-of-function allele of *dia* can be suppressed by Mrtf overexpression in NSCs, suggesting that Dia-Mrtf signaling plays an important role during brain development.

F-actin dynamics controls cell proliferation via SRF-MRTF signaling in vascular smooth muscle cells, where SRF-MRTF signaling activates the transcription of cell proliferation regulators such as connective tissue growth factor (*92*). We propose that in qNSCs, F-actin dynamics controls NSC reactivation via SRF-MRTF signaling. We speculate that Mrtf might directly target genes that are required for NSC reactivation. In addition, F-actin dynamics might be important for cell growth of qNSCs during their reactivation. *Akt*, a component of Drosophila Insulin-like receptor (dInR)–phosphatidylinositol 3-kinase–Akt pathway that controls qNSC reactivation in larval brain of *Drosophila* (*5*, *6*), was among the known target genes of Mrtf in *Drosophila* egg chambers (*56*). However, Akt protein levels remained unaltered in $Mrtf^{\Delta 7}$ NSCs (fig. S18, C and D). Further studies are required to better understand how F-actin dynamic–mediated Mrtf signaling regulates NSC reactivation during brain development, including identifying its direct targets besides actin.

Astrocytes function as a new niche to promote quiescence exit of NSCs

Surface glial cells form the BBB in *Drosophila* larval brains and function as an NSC niche to secrete insulin-like peptides that activate qNSCs (*5*). In the mammalian brain, astrocytes contact and surround the BBB, made of endothelial cells, to regulate its permeability; astrocytes also secrete factors including transforming growth factor–β, glial cell line–derived neurotrophic factor, and fibroblast growth factor to regulate NSC quiescence, proliferation, and differentiation (*93*–*98*). In this study, we have established that astrocytes, a subtype of glial cells, function as a new NSC niche that promotes NSC reactivation in *Drosophila* larval brains. This astrocyte niche functions independently of the previously known niche, the BBB glial cells. The BBB (surface glial cells) in *Drosophila* is located at the surface of the larval brain, close to the cell body of qNSCs, while astrocytes are located at the neuropil surface, the inner part of the larval brain that comes in contact with the tip of the primary protrusion of qNSCs. Therefore, *Drosophila* qNSCs appear to be interposed between two niches, the BBB glia and astrocytes, for their reactivation. Further, astrocytes produce the ligand Fog, which activates the GPCR Smog signaling pathway in NSCs for their reactivation. As astrocytes-derived Fog signaling is independent of nutritional conditions, Fog/Smog-mediated control of actin dynamics may prime NSCs for reactivation in response to nutritional cues. This study proposes an avenue to manipulate astrocytes and the GPCR

signaling pathway to control NSC behavior for the potential treatment of neurodevelopmental disorders.

MATERIALS AND METHODS

Fly stocks and culture

Drosophila stocks were cultured at 22° to 25°C on standard medium. *Yellow white (yw)* and *UAS–β-gal RNAi* were used as WT and Upstream Activation Sequence (UAS) controls for most experiments. The following fly strains were used in this study: *grh-GAL4* (a gift from A. Brand laboratory), *repo-GAL4* (BDSC, #7415), *dia*^{1} (BDSC, #11762), *dia*^{5} (BDSC, #9138), *Df(2L)ED1317* (*dia* deficiency; BDSC, #9175), *Gα*$_q^{221C}$ (BDSC, #30744), *Df(2R)Gα*$_q$*1.3* (*Gα*$_q$ deficiency; BDSC, #44611), *bs[03267]* (BDSC, #83157), *Df(2R)Exel6082* (*bs* deficiency; BDSC, #7561), *mrtf[Delta7]* (BDSC, #58418), *Df(3L)BSC412* (*mrtf* deficiency; BDSC, #24916), Df(2L)Exel9062 (*smog* deficiency;, BDSC, #7792), *smog*^{KO} (a gift from T. Lecuit laboratory), *smog*[CR00977-TG4.0] (*smog-GAL4*; BDSC, #83229), *sqhP>Smog::GFP* (a gift from T. Lecuit laboratory), *NP6293-GAL4* (Drosophila Genomics Resource Center, #105-188), NP2276-GAL4 (Drosophila Genomics Resource Center, #112-853), *nrv2*-GAL4 (BDSC, #6797), and *alrm*-GAL4 (BDSC, #67032). Flies carrying UAS-RNAi or UAS-transgenes were cultured at 29° or 31°C to enhance the efficiency of gene inhibition or the expression of genes. UAS-RNAi or UAS-transgene lines used in this study are listed as follows: *UAS-GFP-Moesin* (BDSC, #31776), *UAS-GFP-UtABD* (a gift from T. Lecuit laboratory), *UAS–β-Gal RNAi* (BDSC, #50680), *UAS-dia RNAi-1* (BDSC, #33424), *UAS-dia RNAi-2* (BDSC, #35479), *UAS-Gα*$_q$ *RNAi-1* (BDSC, #33765), *UAS-Gα*$_q$ *RNAi-2* [Vienna Drosophila Resource Center (VDRC), # 105300], *UAS-Gα*$_q^{Q203L}$ (BDSC, #30743), *UAS-rho1 RNAi-1* (BDSC, #9909), *UAS-rho1 RNAi-2* (BDSC, #9910), *UAS-GFP::Rho1* (BDSC, #9393), *UAS-Rho1*^{N19} (BDSC, #58818), *UAS-DiaRBD-GFP* (BDSC, #52291), *UAS-Dia::EGFP* (BDSC, #56751), *UAS-bs RNAi-1* (VDRC, #330226), *UAS-bs RNAi-2* (BDSC, #26755), *UAS-mrtf RNAi-1* (BDSC, #31930), *UAS-mrtf RNAi-2* (BDSC, #42537), *UAS-mrtf* (BDSC, #58421), *UAS-smog RNAi-1* (BDSC, #43135), *UAS-smog RNAi-2* (BDSC, #51705), *UAS-mist RNAi-1* (BDSC, #41930), *UAS-mist RNAi-2* (BDSC, #57699), *UAS-cta RNAi-1* (BDSC, #41964), *UAS-cta RNAi-2* (BDSC, #51849), *UAS-GABA*$_B$*-R1 RNAi-1* (BDSC, #28353), *UAS- GABA*$_B$*-R1 RNAi-2* (BDSC, #51817), *UAS-wts RNAi* (BDSC, #34064), *UAS-yki-S168A-GFP* (BDSC, #28836), *UAS-Gα*$_q^{WT}$ (a gift from W. Hu laboratory), *UAS-fog RNAi-1* (BDSC, #36970), *UAS-fog RNAi-2* (BDSC, #61917), *UAS-Shibir*^{K44A} (BDSC, #5811), *UAS-spir RNAi-1* (BDSC, #61283), *UAS-spir RNAi-2* (BDSC, #30516), *UAS-chic RNAi-1* (VDRC, #102579), *UAS-chic RNAi-2* (BDSC, #34523), *UAS-sn RNAi-1* (BDSC, #42615), *UAS-sn RNAi-2* (BDSC, #57805), *UAS-Capulet* (BDSC, #5943), *UAS-Cpb-mCherry* (BDSC, #58727), *UAS-Tsr.N* (BDSC, #9234), *UAS-TsrS3A* (BDSC, #9236), *UAS-tsr RNAi-1* (VDRC, #110599), *UAS-tsr RNAi-2* (BDSC, #65055), *UAS-capulet RNAi-1* (BDSC, #21995), *UAS-capulet RNAi-2* (BDSC, #33010), *UAS-cpb RNAi-1* (BDSC, #41952), *UAS-cpb RNAi-2* (BDSC, #26298), *UAS-Tsr-S3E* (BDSC, #9238), *UAS-Arp2 RNAi-1* (VDRC, #29944), *UAS-Arp2 RNAi-2* (VDRC, #101999), *UAS-Arp3 RNAi-1* (BDSC, #53972), *UAS-Arp3 RNAi-2* (BDSC, #32921), *UAS-WASp RNAi-1* (BDSC, #25955), and *UAS-WASp RNAi-2* (BDSC, #51802).

Immunohistochemistry

Immunostaining of *Drosophila* larval brain was performed as previously described (*99*). Briefly, the brains were dissected in phosphate-buffered saline (PBS) and then fixed in 4% (v/v) of formaldehyde / PBS for 22 min at room temperature. Fixed brains were washed three times with 0.3% PBST (0.3% Triton X-100 in PBS) (10 min each on rotator), blocked with 3% bovine serum albumin (BSA) in 0.3% PBST for 1 hour at room temperature, and then incubated with primary antibodies in 3% BSA (in 0.3% PBST) overnight at 4°C. After washing with 0.3% PBST thrice, the brains were then incubated with secondary antibodies in 0.3% PBST for 1.5 hours at room temperature on a rotator. DNA was labeled with ToPro-3 (1:5000; Invitrogen, catalog no. T3605) in 0.3% PBST for 30 min at room temperature. After washing with 0.3% PBST twice, the brains were mounted in mounting medium. The images were collected on a Zeiss LSM 710 confocal microscope (Axio Observer Z1, ZEISS) using a Plan-Apochromat 40×/1.3 NA (numerical aperture) oil differential interference contrast objective. They were then processed with Zen software (2010 version), Fuji ImageJ, and Adobe Photoshop (V24.1.1) software.

The following primary antibodies were used: guinea pig anti-deadpan (Dpn; 1:1000), mouse anti-Miranda (Mira; 1:50; F. Matsuzaki), rabbit anti-GFP (1:3000; F. Yu), mouse anti-GFP (1:5000; F. Yu), rabbit anti-Dia (1:5000; S. Wasserman), rabbit anti–red fluorescent protein (RFP) (1:2000), rabbit anti-Yki (1:50), rabbit anti-Fog antibody (1:200; N. Fuse), rabbit anti-Mrtf antibody (1:200), mouse anti-Repo antibody (1:20; Developmental Studies Hybridoma Bank, catalog no. 8D12), mouse anti-Pros antibody (1:10; Developmental Studies Hybridoma Bank, catalog no. MR1A), and rabbit anti-Akt antibody (1:100; Cell Signaling Technology, catalog no. 4691S). The secondary antibodies used were conjugated with Alexa Fluor 488, Alexa Fluor 555, or Alexa Fluor 647 (the Jackson Laboratory).

Rhodamine phalloidin (1:200; Invitrogen, catalog no. 415) was used to label F-actin. The larval brains were dissected in PBS and fixed in 4% (v/v) of formaldehyde/PBS for 22 min at room temperature, following which the fixed brains were washed with 0.1% PBST thrice (10 min each on a rotator). The brains were then blocked with 3% BSA in 0.1% PBST for 1 hour at room temperature and incubated with primary antibodies in 3% BSA (in 0.1% PBST) overnight at 4°C. After washing with 0.1% PBST thrice, the brains were incubated with rhodamine phalloidin and secondary antibodies in 0.1% PBST for 1.5 hours at room temperature on a rotator. Last, the brains were mounted in mounting medium. For protein signals measured within the protrusion, the focal plane with the strongest fluorescent signals of the protein of interest was selected for quantification.

EdU incorporation assay

Drosophila larvae were fed with food containing 0.2 mM EdU from Click-iT EdU Imaging Kits (Invitrogen, catalog no. C10638) for 4 hours before dissection. The brains were dissected in PBS and fixed with 4% formaldehyde in PBS for 22 min, followed by standard immunohistochemistry. After incubation with secondary antibodies, the brains were washed three times with 0.3% PBST (10 min each), followed by detection of incorporated EdU according to the manufacturers' protocol.

Expansion microscopy–structure illumination microscopy

Drosophila larval brains at 6-hour ALH were dissected in PBS, following which they were immunostained as described above. After staining, the brains were incubated in the anchoring solution Acryloyl-X SE—Acryloyl-X SE (0.1 mg/ml) in 100 mM MES and 150 mM NaCl (pH 6.0)—at 4°C overnight. Next, the samples were incubated in the gelation solution—2 M NaCl, 8.6% sodium acrylate, 2.5% acrylamide, 0.15% bisacrylamide, 0.01% 4-hydroxy-2,2,6,6-tetrame

nthyl-piperidin-1-oxyl, 0.2% tetramethylethylenediamine, and 0.2% ammonium persulfate in PBS at 4°C for 3 hours, followed by incubation at 37°C for 1 hour for complete gel polymerization. After gelation, polymerized gels were digested with digestion buffer [proteinase K (8 U/ml), 50 mM tris (pH 8), 1 mM EDTA, and 0.5% Triton X-100 in water) on a shaker at room temperature for 2 hours. Gels were trimmed to small pieces. Small gel pieces were expanded by incubating them in Milli-Q water for 6 hours at room temperature, which increased gel size to about four times their original size. The expanded gels were examined using super-resolution SIM.

The super-resolution spinning disk confocal SIM consisted of a spinning disk platform (Gataca Systems) coupled with an inverted microscope (Nikon Ti2-E, Nikon), a confocal spinning head (CSU-W, Yokogawa), a Plan-Apo objective (100×, 1.45 NA), a back-illuminated scientific complementary metal-oxide semiconductor camera (Prime95B, Teledyne Photometrics), and a super-resolution module (Live-SR, Gataca Systems). The system employed a laser combiner (iLAS system, Gataca Systems) that provided excitation light at 488-nm/150-mW (Vortran; for GFP), 561-nm/100-mW (Coherent; for mCherry/mRFP/tagRFP), and 639-nm/150-mW [Vortran; for near-infrared fluorescent protein (iRFP)] wavelengths. All images were acquired and processed using the MetaMorph (Molecular Devices) software, followed by further processing with ImageJ and Adobe Photoshop software (V24.1.1).

Live-cell imaging

Larval brains expressing UAS-GFP-Moe or UAS-GFP-utABD under *grh-GAL4* at 6-hour ALH were dissected in a mixture of Shield and Sang M3 insect medium (Sigma-Aldrich, catalog no. S8398) supplemented with 10% fetal bovine serum (FBS). Following dissection, six to eight larval brains were placed in a single well of an eight-chamber borosilicate cover glass containing stabilization medium [0.3% methylcellulose, 10% FBS, glutathione (0.05 mg/ml), and insulin (320 μg/ml) in M3 medium). To capture time-lapse images of NSCs, a super-resolution spinning disk confocal-SIM equipped with a Plan-Apo objective (100×, 1.45 NA) was used. The imaging was conducted in a chamber at a temperature of 29°C. qNSCs with protrusion attached to the neuropil were imaged for 16 hours (5 to 6 min each time interval). The protrusions of qNSCs were captured with multiple *Z* planes to cover the entire thickness of protrusion, thereby preventing any loss of signals resulting from movement out of the focal plane. The videos were processed using Adobe Photoshop (V24.1.1) and ImageJ software.

Fluorescence recovery after photobleaching

Larval brains expressing UAS-GFP::utABD under *grh-GAL4* at 6-hour ALH were dissected in Shield and Sang M3 insect medium as described in live-cell imaging protocol. FRAP measurements were performed using a laser scanning confocal microscope (40× objective lens and Zoom factor 5) on a Nikon A1R MP. Photobleaching was achieved by focusing 25% 488-nm laser for 8 s on the selected region of interest (ROI) in the middle of the protrusion. Fluorescent images of the cells were acquired before and after photobleaching by time-lapse imaging of qNSCs every 1 s for 5 min. The recovery time of fluorescent intensity in ROI of the cell that were photobleached was measured similar to the laser ablation methodology.

Laser ablation of qNSCs

Larval brains expressing UAS-GFP::utABD under *grh-GAL4* at 6-hour ALH were dissected in Shield and Sang M3 insect medium (Sigma-Aldrich, catalog no. S8398) supplemented with 10% FBS. Dissected brain explants were placed in a well containing M3 medium with 0.3% methylcellulose (see the "Live-cell imaging" section). Live imaging of larval brains was performed on a Nikon A1R MP laser scanning confocal microscope using 40× objective lens and Zoom factor 5. qNSCs with protrusion attached to the neuropil were imaged for 15 min (1 min each interval before ablation). The middle region of the NSC protrusions was severed by a picolaser emitting 100 to 130 nW of laser power for 0.5 to 1 s. After injury, qNSCs were imaged again for 15 min (1 min per interval, 10 to 15 z-stacks with 0.5- to 0.8-μm *z* intervals). Images were processed and analyzed with ImageJ and Adobe Photoshop software (V24.1.1).

Antibody generation

Mrtf antibodies were generated by Abmart (Shanghai, China). The synthetic polypeptides containing the coding sequence of *Drosophila* Mrtf (amino acids 1119 to 1418) were used as an immunogen to boost rabbits. The antibodies were then subjected to affinity purification to obtain purified polyclonal Mrtf antibodies. Yki antibodies were generated by GeneScript. The synthetic polypeptides containing the coding sequence of *Drosophila* Yki (amino acids 180 to 418) were used as an immunogen to boost rabbits. The antibodies were then subjected to affinity purification to obtain purified polyclonal Yki antibodies.

Data analysis of scRNA-seq

Raw data were downloaded from GSE134722 (*59*) and processed by Seurat 4.0. The raw data were firstly analyzed according to the methods in Avalos *et al*. (*59*) to separate clusters of NSCs, glia, and neurons, following which subclustering was performed in the clusters of NSCs and glial cells. Quiescent and active NSCs were annotated by the expression of proliferating markers: *wor*, *CycA*, *CycE*, *PCNA*, etc. Subtypes of glial cells were classified by cell type–specific markers: surface glia: *CG6126* and *Indy*; cortex/chiasm glia: *hoe1* and *wrapper*; astrocyte/neuropil glia: *wun2*, *Eaat1*, and *Gat*. Astrocyte/neuropil glia were further classified into astrocyte-like glia and ensheathing glia by the astrocyte-like glia–specific markers: *e* and *CG31235*.

Extraction of total mRNA and reverse transcription quantitative polymerase chain reaction

Total mRNA was extracted from larval brains of control (yw) and mrtf[Delta7] at 24-hour ALH using TRI Reagent (Sigma-Aldrich) according to the manufacturer's instructions. Reverse transcription (RT) was performed with iScript cDNA Synthesis Kit (Bio-Rad) according to the manufacturer's instructions. RT quantitative polymerase chain reaction (RT-qPCR) was performed according to the manufacturer's instructions (SsoFast EvaGreen, Bio-Rad). Reference genes used as an internal control were as follows: *rp49*/*Rpl32* (ribosomal protein L32), *Sdh* (succinate dehydrogenase), and *Tbp1*/*Rpt5* (regulatory particle triple-A adenosine triphosphatase 5).

The primers pairs used for RT-qPCR were the following: *rp49*, 5′-TGTCCTTCCAGCTTCAAGATGACCATC-3′ (forward) and 5′-CTTGGGCTTGCGCCATTTGTG-3′ (reverse); *sdh*, 5′-GTCTGAAGATGCAGAAGACC-3′ (forward) and 5′-ACAATAGTCATCTGGGCATT-3′ (reverse); *Tbp-1*, 5′-AAGCCCGTGCCCGTATTATG-3′ (forward) and 5′-AAGTCATCCGTGGATCGGGAC-3′ (reverse); *mrtf*, 5′-GAGTCAGCACGTCACTGGAA-3′ (forward) and 5′-ACTCTTTTATGCAGGCGGTG-3′ (reverse); *actin5C*, 5′-GAGCGCGGTTACTCTTTCAC-3′ (forward) and 5′-GCCATCTCCTGCTCAAAGTC-3′ (reverse).

Quantification and statistics

Drosophila larval brains were placed dorsal side up on microscope slides. Confocal z-stacks were taken from the surface to the deep layers of the larval brains (20 to 35 z-stacks with 2- or 3-μm intervals per brain lobe). For each genotype, at least 10 brain lobes were collected for z-stack imaging, quantified by ImageJ, and plotted in GraphPad Prism 8 software (version 8.3.0). *P* values were calculated from two-tailed unpaired Student's *t* test for comparison of two samples. One-way analysis of variance (ANOVA), followed by Sidak's multiple comparisons test, was used for comparison of more than two sample groups. All data are shown as the means ± SD, except for Figs. 4B, 6H, and 8B, which represent means ± SEM. Statistically nonsignificant (ns) denotes $P > 0.05$, * denotes $P < 0.05$, ** denotes $P < 0.01$, *** denotes $P < 0.001$, and **** denotes $P < 0.0001$. At least two technical replicates were performed for each experiment.

Supplementary Materials

This PDF file includes:
Legends for movies S1 to S7
Figs. S1 to S18

Other Supplementary Material for this manuscript includes the following:
Movies S1 to S7

REFERENCES AND NOTES

1. C. T. J. van Velthoven, T. A. Rando, Stem cell quiescence: Dynamism, restraint, and cellular idling. *Cell Stem Cell* **24**, 213–225 (2019).
2. S. W. Lee, G. D. Clemenson, F. H. Gage, New neurons in an aged brain. *Behav. Brain Res.* **227**, 497–507 (2012).
3. D. J. Doobin, S. Kemal, T. J. Dantas, R. B. Vallee, Severe NDE1-mediated microcephaly results from neural progenitor cell cycle arrests at multiple specific stages. *Nat. Commun.* **7**, 12551 (2016).
4. W. Y. Ding, J. Huang, H. Wang, Waking up quiescent neural stem cells: Molecular mechanisms and implications in neurodevelopmental disorders. *PLOS Genet.* **16**, e1008653 (2020).
5. J. M. Chell, A. H. Brand, Nutrition-responsive glia control exit of neural stem cells from quiescence. *Cell* **143**, 1161–1173 (2010).
6. R. Sousa-Nunes, L. L. Yee, A. P. Gould, Fat cells reactivate quiescent neuroblasts via TOR and glial insulin relays in *Drosophila*. *Nature* **471**, 508–512 (2011).
7. M. Juanes, G. Guercio, R. Marino, E. Berensztein, D. M. Warman, M. Ciaccio, S. Gil, M. Bailez, M. A. Rivarola, A. Belgorosky, Three novel IGF1R mutations in microcephalic patients with prenatal and postnatal growth impairment. *Clin. Endocrinol. (Oxf)* **82**, 704–711 (2015).
8. G. Mairet-Coello, A. Tury, E. DiCicco-Bloom, Insulin-like growth factor-1 promotes G_1/S cell cycle progression through bidirectional regulation of cyclins and cyclin-dependent kinase inhibitors via the phosphatidylinositol 3-kinase/Akt pathway in developing rat cerebral cortex. *J. Neurosci.* **29**, 775–788 (2009).
9. H. Song, C. F. Stevens, F. H. Gage, Astroglia induce neurogenesis from adult neural stem cells. *Nature* **417**, 39–44 (2002).
10. M. F. Anderson, M. A. Aberg, M. Nilsson, P. S. Eriksson, Insulin-like growth factor-I and neurogenesis in the adult mammalian brain. *Brain Res. Dev. Brain Res.* **134**, 115–122 (2002).
11. S. Li, C. T. Koe, S. T. Tay, A. L. K. Tan, S. Zhang, Y. Zhang, P. Tan, W. K. Sung, H. Wang, An intrinsic mechanism controls reactivation of neural stem cells by spindle matrix proteins. *Nat. Commun.* **8**, 122 (2017).
12. J. Gil-Ranedo, E. Gonzaga, K. J. Jaworek, C. Berger, T. Bossing, C. S. Barros, STRIPAK members orchestrate hippo and insulin receptor signaling to promote neural stem cell reactivation. *Cell Rep.* **27**, 2921–2933.e5 (2019).
13. J. Huang, H. Wang, Hsp83/Hsp90 physically associates with insulin receptor to promote neural stem cell reactivation. *Stem Cell Rep.* **11**, 883–896 (2018).
14. P. T. Ly, Y. S. Tan, C. T. Koe, Y. Zhang, G. Xie, S. Endow, W. M. Deng, F. Yu, H. Wang, $CRL4^{Mahj}$ E3 ubiquitin ligase promotes neural stem cell reactivation. *PLoS Biol.* **17**, e3000276 (2019).
15. J. Huang, M. R. Gujar, Q. Deng, S. Y Chia, S. Li, P. Tan, W. K. Sung, H. Wang, Histone lysine methyltransferase Pr-set7/SETD8 promotes neural stem cell reactivation. *EMBO Rep.* **22**, e50994 (2021).
16. Q. Deng, Y. S. Tan, L. Y. Chew, H. Wang, Msps governs acentrosomal microtubule assembly and reactivation of quiescent neural stem cells. *EMBO J.* **40**, e104549 (2021).
17. M. R. Gujar, Y. Gao, X. Teng, Q. Deng, K. Y. Lin, Y. S. Tan, Y. Toyama, H. Wang, Golgi-dependent reactivation and regeneration of *Drosophila* quiescent neural stem cells. *Dev. Cell* **58**, 1933–1949.e5 (2023).
18. R. Ding, K. Weynans, T. Bossing, C. S. Barros, C. Berger, The Hippo signalling pathway maintains quiescence in *Drosophila* neural stem cells. *Nat. Commun.* **7**, 10510 (2016).
19. C. L. Poon, K. A. Mitchell, S. Kondo, L. Y. Cheng, K. F. Harvey, The Hippo pathway regulates neuroblasts and brain size in *Drosophila melanogaster*. *Curr. Biol.* **26**, 1034–1042 (2016).
20. B. LaFoya, K. E. Prehoda, Actin-dependent membrane polarization reveals the mechanical nature of the neuroblast polarity cycle. *Cell Rep.* **35**, 109146 (2021).
21. C. H. Oon, K. E. Prehoda, Asymmetric recruitment and actin-dependent cortical flows drive the neuroblast polarity cycle. *eLife* **8**, e45815 (2019).
22. P. Aspenstrom, Formin-binding proteins: Modulators of formin-dependent actin polymerization. *Biochim. Biophys. Acta* **1803**, 174–182 (2010).
23. A. Al-Maawali, B. J. Barry, A. Rajab, M. El-Quessny, A. Seman, S. N. Coury, A. J. Barkovich, E. Yang, C. A. Walsh, G. H. Mochida, J. M. Stoler, Novel loss-of-function variants in DIAPH1 associated with syndromic microcephaly, blindness, and early onset seizures. *Am. J. Med. Genet. A* **170A**, 435–440 (2016).
24. A. G. Ercan-Sencicek, S. Jambi, D. Franjic, S. Nishimura, M. Li, P. el-Fishawy, T. M. Morgan, S. J. Sanders, K. Bilguvar, M. Suri, M. H. Johnson, A. R. Gupta, Z. Yuksel, S. Mane, E. Grigorenko, M. Picciotto, A. S. Alberts, M. Gunel, N. Šestan, M. W. State, Homozygous loss of DIAPH1 is a novel cause of microcephaly in humans. *Eur. J. Hum. Genet.* **23**, 165–172 (2015).
25. S. Azam, M. E. Haque, M. Jakaria, S. H. Jo, I. S. Kim, D. K. Choi, G-protein-coupled receptors in CNS: A potential therapeutic target for intervention in neurodegenerative disorders and associated cognitive deficits. *Cells* **9**, 506 (2020).
26. P. G. de Oliveira, M. L. S. Ramos, A. J. Amaro, R. A. Dias, S. I. Vieira, $G_{i/o}$-protein coupled receptors in the aging brain. *Front. Aging Neurosci.* **11**, 89 (2019).
27. D. Marafi, T. Mitani, S. Isikay, J. Hertecant, M. Almannai, K. Manickam, R. Abou Jamra, A. W. el-Hattab, J. Rajah, J. M. Fatih, H. du, E. Karaca, Y. Bayram, J. Punetha, J. A. Rosenfeld, S. N. Jhangiani, E. Boerwinkle, Z. C. Akdemir, S. Erdin, J. V. Hunter, R. A. Gibbs, D. Pehlivan, J. E. Posey, J. R. Lupski, Biallelic GRM7 variants cause epilepsy, microcephaly, and cerebral atrophy. *Ann. Clin. Transl. Neurol.* **7**, 610–627 (2020).
28. J. Snedeker, W. J. Gibbons, D. F. Paulding, Z. Abdelhamed, D. R. Prows, R. W. Stottmann, Gpr63 is a modifier of microcephaly in Ttc21b mouse mutants. *PLOS Genet.* **15**, e1008467 (2019).
29. M. Vezain, M. Lecuyer, M. Rubio, V. Dupé, L. Ratié, V. David, L. Pasquier, S. Odent, S. Coutant, I. Tournier, L. Trestard, H. Adle-Biassette, D. Vivien, T. Frébourg, B. J. Gonzalez, A. Laquerrière, P. Saugier-Veber, A de novo variant in ADGRL2 suggests a novel mechanism underlying the previously undescribed association of extreme microcephaly with severely reduced sulcation and rhombencephalosynapsis. *Acta Neuropathol. Commun.* **6**, 109 (2018).
30. S. Lutz, A. Shankaranarayanan, C. Coco, M. Ridilla, M. R. Nance, C. Vettel, D. Baltus, C. R. Evelyn, R. R. Neubig, T. Wieland, J. J. G. Tesmer, Structure of $G\alpha_q$-p63RhoGEF-RhoA complex reveals a pathway for the activation of RhoA by GPCRs. *Science* **318**, 1923–1927 (2007).
31. D. Spiering, L. Hodgson, Dynamics of the Rho-family small GTPases in actin regulation and motility. *Cell Adh. Migr.* **5**, 170–180 (2011).
32. A. S. Hauser, M. M. Attwood, M. Rask-Andersen, H. B. Schioth, D. E. Gloriam, Trends in GPCR drug discovery: New agents, targets and indications. *Nat. Rev. Drug Discov.* **16**, 829–842 (2017).
33. M. G. Gustafsson, Nonlinear structured-illumination microscopy: Wide-field fluorescence imaging with theoretically unlimited resolution. *Proc. Natl. Acad. Sci. U.S.A.* **102**, 13081–13086 (2005).
34. F. Chen, P. W. Tillberg, E. S. Boyden, Optical imaging. Expansion microscopy. *Science* **347**, 543–548 (2015).
35. C. H. Oon, K. E. Prehoda, Phases of cortical actomyosin dynamics coupled to the neuroblast polarity cycle. *eLife* **10**, e66574 (2021).
36. K. Kono, S. Yoshiura, I. Fujita, Y. Okada, A. Shitamukai, T. Shibata, F. Matsuzaki, Reconstruction of Par-dependent polarity in apolar cells reveals a dynamic process of cortical polarization. *eLife* **8**, e45559 (2019).
37. M. P. Bostock, A. R. Prasad, R. Chaouni, A. C. Yuen, R. Sousa-Nunes, M. Amoyel, V. M. Fernandes, An immobilization technique for long-term time-lapse imaging of explanted *Drosophila* tissues. *Front. Cell Dev. Biol.* **8**, 590094 (2020).
38. X. Li, P. Lai, K. Cheng, D. Wang, Genetic analysis of microcephaly-cortical blind syndrome due to compound heterozygous variants of DIAPH1 gene. *Zhonghua Yi Xue Yi Chuan Xue Za Zhi* **39**, 1116–1119 (2022).
39. G. Vazquez-Victorio, C. Gonzalez-Espinosa, Z. P. Espinosa-Riquer, M. Macias-Silva, GPCRs and actin-cytoskeleton dynamics. *Methods Cell Biol.* **132**, 165–188 (2016).

40. N. Mizuno, H. Kokubu, M. Sato, A. Nishimura, J. Yamauchi, H. Kurose, H. Itoh, G protein-coupled receptor signaling through Gq and JNK negatively regulates neural progenitor cell migration. *Proc. Natl. Acad. Sci. U.S.A.* **102**, 12365–12370 (2005).
41. D. H. Castrillon, S. A. Wasserman, Diaphanous is required for cytokinesis in *Drosophila* and shares domains of similarity with the products of the limb deformity gene. *Development* **120**, 3367–3377 (1994).
42. A. D. DeWard, A. S. Alberts, Ubiquitin-mediated degradation of the formin mDia2 upon completion of cell division. *J. Biol. Chem.* **284**, 20061–20069 (2009).
43. S. Kuhn, M. Geyer, Formins as effector proteins of Rho GTPases. *Small GTPases* **5**, e29513 (2014).
44. M. A. Booden, D. P. Siderovski, C. J. Der, Leukemia-associated Rho guanine nucleotide exchange factor promotes Gαq-coupled activation of RhoA. *Mol. Cell. Biol.* **22**, 4053–4061 (2002).
45. H. Chikumi, J. Vazquez-Prado, J. M. Servitja, H. Miyazaki, J. S. Gutkind, Potent activation of RhoA by $G\alpha_q$ and G_q-coupled receptors. *J. Biol. Chem.* **277**, 27130–27134 (2002).
46. D. Toksoz, K. D. Merdek, The Rho small GTPase: Functions in health and disease. *Histol. Histopathol.* **17**, 915–927 (2002).
47. M. T. Abreu-Blanco, J. M. Verboon, S. M. Parkhurst, Coordination of Rho family GTPase activities to orchestrate cytoskeleton responses during cell wound repair. *Curr. Biol.* **24**, 144–155 (2014).
48. L. Sansores-Garcia, W. Bossuyt, K. I. Wada, S. Yonemura, C. Tao, H. Sasaki, G. Halder, Modulating F-actin organization induces organ growth by affecting the Hippo pathway. *EMBO J.* **30**, 2325–2335 (2011).
49. Y. C. Chang, J. W. Wu, C. W. Wang, A. C. Jang, Hippo signaling-mediated mechanotransduction in cell movement and cancer metastasis. *Front. Mol. Biosci.* **6**, 157 (2019).
50. J. W. Copeland, R. Treisman, The diaphanous-related formin mDia1 controls serum response factor activity through its effects on actin polymerization. *Mol. Biol. Cell* **13**, 4088–4099 (2002).
51. J. O. Onuh, H. Qiu, Serum response factor-cofactor interactions and their implications in disease. *FEBS J.* **288**, 3120–3134 (2021).
52. N. T. Rahman, V. P. Schulz, L. Wang, P. G. Gallagher, O. Denisenko, F. Gualdrini, C. Esnault, D. S. Krause, MRTFA augments megakaryocyte maturation by enhancing the SRF regulatory axis. *Blood Adv.* **2**, 2691–2703 (2018).
53. F. Miralles, G. Posern, A. I. Zaromytidou, R. Treisman, Actin dynamics control SRF activity by regulation of its coactivator MAL. *Cell* **113**, 329–342 (2003).
54. K. Somogyi, P. Rorth, Evidence for tension-based regulation of *Drosophila* MAL and SRF during invasive cell migration. *Dev. Cell* **7**, 85–93 (2004).
55. Z. Han, X. Li, J. Wu, E. N. Olson, A myocardin-related transcription factor regulates activity of serum response factor in *Drosophila*. *Proc. Natl. Acad. Sci. U.S.A.* **101**, 12567–12572 (2004).
56. L. Salvany, J. Muller, E. Guccione, P. Rorth, The core and conserved role of MAL is homeostatic regulation of actin levels. *Genes Dev.* **28**, 1048–1053 (2014).
57. E. I. Ramos, G. A. Bien-Willner, J. Li, A. E. O. Hughes, J. Giacalone, S. Chasnoff, S. Kulkarni, M. Parmacek, F. S. Cole, T. E. Druley, Genetic variation in MKL2 and decreased downstream PCTAIRE1 expression in extreme, fatal primary human microcephaly. *Clin. Genet.* **85**, 423–432 (2014).
58. J. Li, L. Wang, H. Guo, L. Shi, K. Zhang, M. Tang, S. Hu, S. Dong, Y. Liu, T. Wang, P. Yu, X. He, Z. Hu, J. Zhao, C. Liu, Z. S. Sun, K. Xia, Targeted sequencing and functional analysis reveal brain-size-related genes and their networks in autism spectrum disorders. *Mol. Psychiatry* **22**, 1282–1290 (2017).
59. C. B. Avalos, G. L. Maier, R. Bruggmann, S. G. Sprecher, Single cell transcriptome atlas of the *Drosophila* larval brain. *eLife* **8**, e50354 (2019).
60. L. Khrimian, A. Obri, M. Ramos-Brossier, A. Rousseaud, S. Moriceau, A. S. Nicot, P. Mera, S. Kosmidis, T. Karnavas, F. Saudou, X. B. Gao, F. Oury, E. Kandel, G. Karsenty, Gpr158 mediates osteocalcin's regulation of cognition. *J. Exp. Med.* **214**, 2859–2873 (2017).
61. S. Kerridge, A. Munjal, J. M. Philippe, A. Jha, A. G. de las Bayonas, A. J. Saurin, T. Lecuit, Modular activation of Rho1 by GPCR signalling imparts polarized myosin II activation during morphogenesis. *Nat. Cell Biol.* **18**, 261–270 (2016).
62. V. Vishwakarma, T. P. Le, S. Chung, Multifunctional role of GPCR signaling in epithelial tube formation. *Development* **149**, dev200519 (2022).
63. V. Hartenstein, Morphological diversity and development of glia in *Drosophila*. *Glia* **59**, 1237–1252 (2011).
64. V. Katagade, M. Kandroo, A. Ratnaparkhi, Embryonic spatio-temporal expression pattern of folded gastrulation (Fog) suggests roles in multiple morphogenetic events and regulation by AbdA. *G3 (Bethesda)* **7**, jkae032 (2024).
65. R. E. Dawes-Hoang, K. M. Parmar, A. E. Christiansen, C. B. Phelps, A. H. Brand, E. F. Wieschaus, Folded gastrulation, cell shape change and the control of myosin localization. *Development* **132**, 4165–4178 (2005).
66. N. Chakrabarty, P. Dubey, Y. Tang, A. Ganguly, K. Ladt, C. Leterrier, P. Jung, S. Roy, Processive flow by biased polymerization mediates the slow axonal transport of actin. *J. Cell Biol.* **218**, 112–124 (2019).
67. A. Ganguly, Y. Tang, L. Wang, K. Ladt, J. Loi, B. Dargent, C. Leterrier, S. Roy, A dynamic formin-dependent deep F-actin network in axons. *J. Cell Biol.* **210**, 401–417 (2015).
68. K. Xu, G. Zhong, X. Zhuang, Actin, spectrin, and associated proteins form a periodic cytoskeletal structure in axons. *Science* **339**, 452–456 (2013).
69. F. Lavoie-Cardinal, A. Bilodeau, M. Lemieux, M. A. Gardner, T. Wiesner, G. Laramée, C. Gagné, P. de Koninck, Neuronal activity remodels the F-actin based submembrane lattice in dendrites but not axons of hippocampal neurons. *Sci. Rep.* **10**, 11960 (2020).
70. P. Speder, A. H. Brand, Gap junction proteins in the blood-brain barrier control nutrient-dependent reactivation of *Drosophila* neural stem cells. *Dev. Cell* **30**, 309–321 (2014).
71. K. M. Pearce, M. Bell, W. H. Linthicum, Q. Wen, J. Srinivasan, P. Rangamani, S. Scarlata, Gαq-mediated calcium dynamics and membrane tension modulate neurite plasticity. *Mol. Biol. Cell* **31**, 683–694 (2020).
72. P. Forscher, S. J. Smith, Actions of cytochalasins on the organization of actin filaments and microtubules in a neuronal growth cone. *J. Cell Biol.* **107**, 1505–1516 (1988).
73. E. Tanaka, J. Sabry, Making the connection: Cytoskeletal rearrangements during growth cone guidance. *Cell* **83**, 171–176 (1995).
74. V. A. Doze, D. M. Perez, GPCRs in stem cell function. *Prog. Mol. Biol. Transl. Sci.* **115**, 175–216 (2013).
75. J. R. Lynch, J. Y. Wang, G protein-coupled receptor signaling in stem cells and cancer. *Int. J. Mol. Sci.* **17**, 707 (2016).
76. A. J. Manning, K. A. Peters, M. Peifer, S. L. Rogers, Regulation of epithelial morphogenesis by the G protein-coupled receptor mist and its ligand Fog. *Sci. Signal.* **6**, ra98 (2013).
77. A. J. Manning, S. L. Rogers, The Fog signaling pathway: Insights into signaling in morphogenesis. *Dev. Biol.* **394**, 6–14 (2014).
78. P. Morize, A. E. Christiansen, M. Costa, S. Parks, E. Wieschaus, Hyperactivation of the folded gastrulation pathway induces specific cell shape changes. *Development* **125**, 589–597 (1998).
79. A. Karls, M. Mynlieff, $GABA_B$ receptors couple to $G\alpha_q$ to mediate increases in voltage-dependent calcium current during development. *J. Neurochem.* **135**, 88–100 (2015).
80. L. P. Sutton, C. Orlandi, C. Song, W. C. Oh, B. S. Muntean, K. Xie, A. Filippini, X. Xie, R. Satterfield, J. D. W. Yaeger, K. J. Renner, S. M. Young Jr., B. Xu, H. Kwon, K. A. Martemyanov, Orphan receptor GPR158 controls stress-induced depression. *eLife* **7**, e33273 (2018).
81. D. Cetereisi, I. Kramvis, T. Gebuis, R. J. van der Loo, Y. Gouwenberg, H. D. Mansvelder, K. W. Li, A. B. Smit, S. Spijker, Gpr158 deficiency impacts hippocampal CA1 neuronal excitability, dendritic architecture, and affects spatial learning. *Front. Cell. Neurosci.* **13**, 465 (2019).
82. C. Bichsel, J. Bischoff, A somatic missense mutation in GNAQ causes capillary malformation. *Curr. Opin. Hematol.* **26**, 179–184 (2019).
83. L. Huang, J. A. Couto, A. Pinto, S. Alexandrescu, J. R. Madsen, A. K. Greene, M. Sahin, J. Bischoff, Somatic GNAQ mutation is enriched in brain endothelial cells in Sturge-weber syndrome. *Pediatr. Neurol.* **67**, 59–63 (2017).
84. M. D. Shirley, H. Tang, C. J. Gallione, J. D. Baugher, L. P. Frelin, B. Cohen, P. E. North, D. A. Marchuk, A. M. Comi, J. Pevsner, Sturge-Weber syndrome and port-wine stains caused by somatic mutation in GNAQ. *N. Engl. J. Med.* **368**, 1971–1979 (2013).
85. D. Herzog, P. Loetscher, J. van Hengel, S. Knüsel, C. Brakebusch, V. Taylor, U. Suter, J. B. Relvas, The small GTPase RhoA is required to maintain spinal cord neuroepithelium organization and the neural stem cell pool. *J. Neurosci.* **31**, 5120–5130 (2011).
86. Z. R. Cai, C. McCuaig, A. Hatami, J. B. Riviere, D. Marcoux, A novel pathogenic RHOA variant in a patient with patterned cutaneous hypopigmentation associated with extracutaneous findings. *Pediatr. Dermatol.* **39**, 281–287 (2022).
87. P. Vabres, A. Sorlin, S. S. Kholmanskikh, B. Demeer, J. St-Onge, Y. Duffourd, P. Kuentz, J. B. Courcet, V. Carmignac, P. Garret, D. Bessis, O. Boute, A. Bron, G. Captier, E. Carmi, B. Devauchelle, D. Geneviève, C. Gondry-Jouet, L. Guibaud, A. Lafon, M. Mathieu-Dramard, J. Thevenon, W. B. Dobyns, G. Bernard, S. Polubothu, F. Faravelli, V. A. Kinsler, C. Thauvin, L. Faivre, M. E. Ross, J. B. Rivière, Postzygotic inactivating mutations of RHOA cause a mosaic neuroectodermal syndrome. *Nat. Genet.* **51**, 1438–1441 (2019).
88. G. Lian, A. Chenn, V. Ekuta, S. Kanaujia, V. Sheen, Formin 2 regulates lysosomal degradation of Wnt-associated β-catenin in neural progenitors. *Cereb. Cortex* **29**, 1938–1952 (2019).
89. F. Gualdrini, C. Esnault, S. Horswell, A. Stewart, N. Matthews, R. Treisman, SRF co-factors control the balance between cell proliferation and contractility. *Mol. Cell* **64**, 1048–1061 (2016).
90. O. M. Yu, S. Miyamoto, J. H. Brown, Myocardin-related transcription factor a and yes-associated protein exert dual control in G protein-coupled receptor- and RhoA-mediated transcriptional regulation and cell proliferation. *Mol. Cell. Biol.* **36**, 39–49 (2016).
91. Y. Wang, P. Min, C. Qi, S. Zhao, M. Yu, Y. Zhang, J. du, MICAL2 facilitates gastric cancer cell migration via MRTF-A-mediated CDC42 activation. *Front. Mol. Biosci.* **8**, 568868 (2021).
92. M. C. McNeill, J. Wray, G. B. Sala-Newby, C. C. T. Hindmarch, S. A. Smith, R. Ebrahimighaei, A. C. Newby, M. Bond, Nuclear actin regulates cell proliferation and

migration via inhibition of SRF and TEAD. *Biochim. Biophys. Acta Mol. Cell Res.* **1867**, 118691 (2020).
93. L. Luo, K. Guo, W. Fan, Y. Lu, L. Chen, Y. Wang, Y. Shao, G. Wu, J. Xu, L. Lü, Niche astrocytes promote the survival, proliferation and neuronal differentiation of co-transplanted neural stem cells following ischemic stroke in rats. *Exp. Ther. Med.* **13**, 645–650 (2017).
94. F. Casse, K. Richetin, N. Toni, Astrocytes' contribution to adult neurogenesis in physiology and Alzheimer's disease. *Front. Cell. Neurosci.* **12**, 432 (2018).
95. Y. Zhou, A. M. Bond, J. E. Shade, Y. Zhu, C. H. O. Davis, X. Wang, Y. Su, K. J. Yoon, A. T. Phan, W. J. Chen, J. H. Oh, N. Marsh-Armstrong, K. Atabai, G. L. Ming, H. Song, Autocrine Mfge8 signaling prevents developmental exhaustion of the adult neural stem cell pool. *Cell Stem Cell* **23**, 444–452.e4 (2018).
96. E. D. Kirby, S. E. Muroy, W. G. Sun, D. Covarrubias, M. J. Leong, L. A. Barchas, D. Kaufer, Acute stress enhances adult rat hippocampal neurogenesis and activation of newborn neurons via secreted astrocytic FGF2. *eLife* **2**, e00362 (2013).
97. S. Boku, S. Nakagawa, N. Takamura, A. Kato, M. Takebayashi, K. Hisaoka-Nakashima, Y. Omiya, T. Inoue, I. Kusumi, GDNF facilitates differentiation of the adult dentate gyrus-derived neural precursor cells into astrocytes via STAT3. *Biochem. Biophys. Res. Commun.* **434**, 779–784 (2013).
98. P. D. Radice, P. Mathieu, M. C. Leal, M. I. Farías, C. Ferrari, M. Puntel, M. Salibe, A. Chernomoretz, F. J. Pitossi, Fibulin-2 is a key mediator of the pro-neurogenic effect of TGF-beta1 on adult neural stem cells. *Mol. Cell. Neurosci.* **67**, 75–83 (2015).
99. C. T. Koe, S. Li, F. Rossi, J. J. L. Wong, Y. Wang, Z. Zhang, K. Chen, S. S. Aw, H. E. Richardson, P. Robson, W. K. Sung, F. Yu, C. Gonzalez, H. Wang, The Brm-HDAC3-Erm repressor complex suppresses dedifferentiation in *Drosophila* type II neuroblast lineages. *eLife* **3**, e01906 (2014).

Acknowledgments: We thank A. Brand, T. Lecuit, F. Matsuzaki, S. Wasserman, N. Fuse, W. Hu, A. Ratnaparkhi, and F. Yu; the Bloomington Drosophila Stock Center; VDRC; Kyoto Stock Centre DGGR; the Developmental Studies Hybridoma Bank for fly stocks and antibodies; and H.-J. Hsu for comments on this manuscript. The working model was created with BioRender. **Funding:** This work is supported by the Ministry of Health, Singapore; National Medical Research Council, Singapore MOH-000143 (MOH-OFIRG18may-0004) to H.W.; National Medical Research Council, Singapore Open Fund Young Individual Research Grant MOH-001236 (MOH-OFYIRG22jul-0002) and Khoo Postdoctoral Fellowship award (KPFA/2020/0059) to K.-Y.L.; Ministry of Education, Singapore MOE Tier 2 (T2EP30220-0033) to Y.T.; Université de Paris/National University of Singapore grant ANR-18-IDEX-000/2021-03-R/UP-NUS and MBI intramural funding to P.K. **Author contributions:** Conceptualization: K.-Y.L. and H.W.. Methodology: K.-Y.L., M.R.G., J.L., Y.G., Y.S.T., W.Y.D., J.H., X.T., and L.S.L.C. Investigation: K.-Y.L., M.R.G., J.L., Y.G., Y.S.T., W.Y.D., and J.H. Visualization: K.-Y.L. and H.W. Funding acquisition: H.W., K.-Y.L., P.K. and Y.T. Resources: P.K. and H.W. Supervision: H.W. Writing—original draft: K.-Y.L. and H.W. **Competing interests:** The authors declare that they have no competing interests. **Data and materials availability:** All data needed to evaluate the conclusions in the paper are present in the paper and/or the Supplementary Materials.

Submitted 22 October 2023
Accepted 18 June 2024
Published 24 July 2024
10.1126/sciadv.adl4694